PAPER

Check for updates

Engineering of stealth (maghemite/PLGA)/chitosan (core/shell)/shell nanocomposites with potential applications for combined MRI and hyperthermia against cancer

Fátima Fernández-Álvarez, [ID] [a] Carlos Caro, [ID] [b] Gracia García-García, [ID] [ac] María Luisa García-Martín [ID] [bd] and José L. Arias [ID] *[aef]

(Maghemite/poly(D,L-lactide-*co*-glycolide))/chitosan (core/shell)/shell nanoparticles have been prepared reproducibly by nanoprecipitation solvent evaporation plus coacervation (production performance ≈ 45%, average size ≈ 325 nm). Transmission electron microscopy, energy dispersive X-ray spectroscopy, electrophoretic determinations, and X-ray diffraction patterns demonstrated the satisfactory embedment of iron oxide nanocores within the solid polymer matrix and the formation of an external shell of chitosan in the nanostructure. The adequate magnetic responsiveness of the nanocomposites was characterized *in vitro* by hysteresis cycle determinations and by visualization of the nanosystem under the influence of a 0.4 T permanent magnet. Safety and biocompatibility of the (core/shell)/shell particles were based on *in vitro* haemocompatibility studies and cytotoxicity tests against HFF-1 human foreskin fibroblasts and on *ex vivo* toxicity assessments on tissue samples from Balb/c mice. Transversal relaxivities, determined *in vitro* at a low magnetic field of 1.44 T, demonstrated their capability as T_2 contrast agents for magnetic resonance imaging, being comparable to that of some iron oxide-based contrast agents. Heating properties were evaluated in a high frequency alternating electromagnetic gradient: a constant maximum temperature of ≈46 °C was generated within ≈50 min, while antitumour hyperthermia tests on T-84 colonic adenocarcinoma cells proved the relevant decrease in cell viability (to ≈ 39%) when treated with the nanosystem under the influence of that electromagnetic field. Finally, *in vivo* magnetic resonance imaging studies and *ex vivo* histology determinations of iron deposits postulated the efficacy of chitosan to provide long-circulating capabilities to the nanocomposites, retarding nanoparticle recognition by the mononuclear phagocyte system. To our knowledge, this is the first study describing such a type of biocompatible and long-circulating nanoplatform with promising theranostic applications (biomedical imaging and hyperthermia) against cancer.

Introduction

The introduction of Nanotechnology in the cancer arena is actively revolutionizing the management of this worrying and severe disease.[1–4] Talking about chemotherapy, antitumour drugs and/or genes have generated significant therapeutic outcomes (when given alone or in combination regimens), and the formulation of biodegradable and biocompatible nanoparticles (NPs) has facilitated the controlled and site-specific delivery of these agents.[5,6] This important input has contributed to overcome the typical problems of cancer chemotherapy (responsible for the use of the high doses inducing acute toxicity):[7,8] (i) unfavourable physical chemistry (*e.g.* hydrophobic character) and pharmacokinetics (rapid metabolism and short plasma half-life) of the active agent; (ii) widespread biodistribution and extravasation in non-targeted areas; (iii) low selectivity toward malignant cells; and (iv) susceptibility to induce chemoresistance in cancer cells.

These barriers have also been described for signal emitters or contrast agents, such as radionuclides, luminophores, or

[a] Department of Pharmacy and Pharmaceutical Technology, Faculty of Pharmacy, University of Granada, Granada, Spain. E-mail: jlarias@ugr.es
[b] Andalusian Centre for Nanomedicine and Biotechnology (BIONAND), Junta de Andalucía–Universidad de Málaga, Málaga, Spain
[c] Faculty of Experimental Sciences, Universidad Francisco de Vitoria, Madrid, Spain
[d] Biomedical Research Networking Center in Bioengineering, Biomaterials and Nanomedicine (CIBER-BBN), Málaga, Spain
[e] Institute of Biopathology and Regenerative Medicine (IBIMER), Center of Biomedical Research (CIBM), University of Granada, Granada, Spain
[f] Biosanitary Research Institute of Granada (ibs.GRANADA), Andalusian Health Service (SAS), University of Granada, Granada, Spain

This journal is © The Royal Society of Chemistry 2021

J. Mater. Chem. B, 2021, **9**, 4963–4980 | **4963**

magnetic resonance imaging (MRI) contrast agents, therefore defining the little sensitivity and limited efficacy of current imaging techniques in the (early) diagnosis and follow-up of cancer. Nanoparticulate systems have been engineered satisfactorily to beat these challenges.[9,10] They even have generated promising results when expanded to alternative treatment options against cancer, *i.e.* hyperthermia,[11,12] photodynamic therapy,[13,14] and photothermal therapy.[15,16]

Introducing passive and active targeting concepts in the engineering of all these nanosystems has been described to optimize their *in vivo* fate (and efficacy).[17,18] Passive targeting strategies, taking advantage of the enhanced permeability and retention (EPR) effect, are based on the formulation of long-circulating or stealth NPs.[19] They are typically prepared by coating the particle surface with a hydrophilic polymer, typically poly(ethylene glycol) (PEG), to protect the NP from opsonization by repelling plasma proteins.[20]

With respect to the active targeting strategies, they are characteristically based on: (i) the surface functionalization of NPs with molecules that can bind selectively to ligands unique to cancer cells (ligand- or receptor-mediated targeting),[21,22] and/or (ii) the engineering of stimuli-sensitive carriers. The latter are NPs that can experience alterations in their structure and physical characteristics under changes in the environment, resulting in the specific (triggered) release of therapeutics at the targeted site.[23,24]

Building nanostructures joining both passive and active targeting functionalities has further resulted in better results in the diagnosis[25] and therapy[26,27] of cancer. Superparamagnetic iron oxides, *e.g.* magnetite (Fe_3O_4) and maghemite (γ-Fe_2O_3), can contribute notably to the formulation of these advanced nanoplatforms, owing to their magnetic targeting capacity,[28–30] in combination with their versatility as agents in both magnetic antitumour hyperthermia[31,32] and MRI.[33,34] As a consequence, they are considered of interest when engineering theranostic NPs against cancer,[29,35,36] in which they can assure MRI contrast, antitumour magnetic hyperthermia, and magnetic targeting and magnetic-based cargo delivery functionalities. The structure of these advanced nanoplatforms based on iron oxides frequently involves a core/shell construction in which the magnetic colloids are embedded in a polymer[37,38] or lipid[39,40] matrix, for the enrichment of their properties, such as colloidal stability, biocompatibility, safety, bioavailability, targeting and controlled release. In this context, poly(D,L-lactide-*co*-glycolide) (PLGA), a Food and Drug Administration (FDA)-approved polymer, demonstrated outstanding applications due to its biocompatibility, biodegradability, and drug vehiculization capabilities (adequate drug loading values along with biphasic controlled drug release properties).[41–43] Remarkably, the latter characteristic includes a pH-triggered drug delivery to the cancer site, given the accelerated degradation of the polymer at the acidic intratumoural pH.[44,45] Furthermore, PLGA has been also proposed to formulate thermoresponsive delivery systems facilitating a heat-triggered drug release at the targeted site.[46–48] All these are the main reasons that could justify the inclusion of the polymer as the inner shell of a (core/shell)/shell nanostructure. As a result, the PLGA shell would provide pH- and heat (hyperthermia)-responsive functionalities to this composite nanoplatform for the selective delivery of therapeutic molecules (drugs and/or genes) to malignant cells. Chitosan (CS) has also been used to prepare biocompatible, biodegradable, and nontoxic magnetic NPs,[37,49–51] providing controlled release of many active agents. This water-soluble, low molecular weight (M_W), biodegradable and biocompatible polymer has recently been proposed as an interesting alternative to PEG chains when engineering stealth NPs. It can provide a hydrophilic stealth coating on NPs to camouflage them from the mononuclear phagocyte system (MPS), thus preventing premature clearance from systemic circulation.[52–54] The positive surface electric charge provided by CS to the NP surface could also contribute to the lack of binding with opsonins, thereby contributing to evading phagocytosis and prolonging blood circulation.[55]

Surface modification of PLGA NPs with a CS shell is possible owing to attractive electrostatic interactions between the negatively charged PLGA particles and the positively charged CS.[56,57] Additional benefits of CS functionalization are the optimization of the sustained drug release capabilities[58–60] and the enhancement of the uptake by targeted cells.[61–64] Therefore, CS surface coating onto these drug- and gene-loaded PLGA nanosystems may help in improving their biodistribution and therapeutic effects.[65,66] This conceptualization has been recently applied to the formulation of magnetopolymer particles, in which a (Fe_3O_4/PLGA)/CS (core/shell)/shell structure was described.[67–69]

In this contribution, we develop a reproducible procedure to formulate (γ-Fe_2O_3/PLGA)/CS NPs. Generation of this (core/shell)/shell nanostructure was evaluated by transmission electron microscopy and elemental analysis, and by comparing the electrical surface properties of the nanocomposite to those of γ-Fe_2O_3/PLGA and CS particles. Mineralogical crystallinity of the γ-Fe_2O_3 nuclei embedded in the polymer matrix was investigated by X-ray diffractometry. Short-term colloidal stability in water was evaluated at 4.0 °C, while magnetic evaluations helped in analysing the magnetic responsiveness. Toxicity assessment was focused on blood compatibility studies, cytotoxicity tests on HFF-1 human foreskin fibroblasts, and haematoxylin and eosin (H&E) staining of tissue samples from Balb/c mice. A preliminary analysis of the potential use of the nanocomposites as MRI contrast agents was accomplished *in vitro*, while their antitumour hyperthermia capabilities were analysed under the influence of a high frequency alternating electromagnetic field in T-84 cells. Finally, *in vivo* distribution of the particles was determined by dynamic MRI and by Prussian blue (PB) visualization of iron deposits in tissue samples.

Materials and methods

Materials

All chemicals were of analytical quality and were used as received without further purification. $Fe(NO_3)_3 \cdot 9H_2O$ (M_W: 404 g mol^{-1}),

$FeCl_2 \cdot 4H_2O$ (M_W: 198.81 g mol^{-1}), KNO_3, $HClO_4$ (70%, American Chemical Society, ACS specification), HCl (37%, ACS specification), EtOH 96°, and CH_3COOH ($\geq$98%, ACS specification) from VWR International, LLC (Spain). Low M_W CS ($\approx$50 000 to 190 000 Da, determined by viscosity measurement; polydispersity not determined by the laboratory; 75–85% deacetylated; 99% purity level), Resomer® RG 502 H [PLGA, 50:50 poly(D,L-lactide):poly(glycolide), $M_W \approx$ 7000 to 17 000 Da, inherent viscosity $\approx$ 0.16 to 0.24 dL g^{-1}], ethylenediaminetetraacetic acid (EDTA), $NaH_2(C_3H_5O$ (COO)$_3$), 4′,6-diamidino-2-phenylindole (DAPI) dihydrochloride, phosphate buffered saline (PBS), 3-(4,5-dimethylthiazol-2-yl)-3,5-diphenyl tetrazolium bromide (MTT) solution, xylene, CH_2O, $K_4[Fe(CN)_6]$, and ethanol 99° from Merck KGaA (Germany). Kolliphor® P-188 from BASF (Germany). $Cl_3FeH_{12}O_6$ (M_W: 270.32 g mol^{-1}), polyvinyl alcohol (PVA, M_W: 72 000 g mol^{-1}), HPLC-grade acetone, and NH_3 (30%, ACS specification) from Panreac (Spain). Na_2SO_4 and oleic acid ($\geq$99%, ACS specification) from Guinama S. L. (Spain). TO-PRO®-3 iodide and dimethyl sulfoxide (DMSO) from ACROS Organics™ (Belgium). Dulbecco's modified Eagle's medium (DMEM), fetal bovine serum (FBS), 2 mM L-glutamine, Gibco™ penicillin–streptomycin solution (100 IU mL^{-1}), and Triton® X-100 from ThermoFisher Scientific Inc. (USA). Deionized and filtered water was used in all the experiments (Milli-Q Academic®, Millipore, France).

Formulation of (γ-Fe₂O₃/PLGA)/CS (core/shell)/shell nanocomposites

Fe_3O_4 NPs were obtained by chemical co-precipitation.[70] The reaction started with the simultaneous and slow addition of 40 mL of 1 M $FeCl_3$ solution and 10 mL of 2 M $FeCl_2$ solution (in 2 M HCl) to 0.5 L of 0.7 M NH_3 solution, at room temperature and under mechanical stirring (700 rpm; IKA® Eurostar 60 Digital Constant-Speed Mixer, Germany). Stirring was continued for 30 min. Long-term stabilization of the Fe_3O_4 particles was then achieved by magnetic isolation (permanent magnet of 0.4 T) from the NH_3 media and re-dispersion in 0.25 L of 2 M $HClO_4$ solution. After 12 h of contact, the NPs were isolated using a magnet (0.4 T), and their oxidation into γ-Fe_2O_3 was accomplished with $Fe(NO_3)_3$ (0.6 L, 0.34 M) at 90 °C during 30 min.[71] Finally, cleaning of the γ-Fe_2O_3 NPs was done by repeated cycles of centrifugation (30 min at 8500 rpm, Centrifuge 5804; Eppendorf Ibérica S. L. U., Spain) until the conductivity of the supernatant was $\leq$10 μS cm^{-1} (Crison Microcm 2202 conductivity meter, Hach Lange Spain S. L. U., Spain).

Incorporation of oleic acid onto the surface of iron oxide NPs has been described to result in a change in the surface characteristics from hydrophilic to hydrophobic.[72,73] This surface transformation in the γ-Fe_2O_3 particles may favour their incorporation into the PLGA matrix when preparing the γ-Fe_2O_3/PLGA (core/shell) particles. To that aim, 3.5 mL of an ethanolic solution of oleic acid (1%, v/v) was added under

sonication (42 kHz sonication frequency, 100 W output power; Bransonic® ultrasonic bath, Branson Ultrasonics Corporation, USA) to 14.25 mg of iron oxide nuclei (1:1.25 iron:oleic molar ratio).[74] Sonication was continued for 60 min. The oleic acid-treated γ-Fe_2O_3 nanocores were isolated from the EtOH solution using a permanent magnet of 0.4 T and washed twice with 1 mL of acetone.

The formulation of the γ-Fe_2O_3/PLGA (core/shell) particles (of 3:4 γ-Fe_2O_3:PLGA weight ratio) was based on the nanoprecipitation solvent evaporation technique, which has been previously used to prepare pure PLGA NPs.[21,75,76] The procedure started with the addition of an organic phase containing PLGA and the oleic acid-modified iron oxide nuclei (19 mg and 14.25 mg in 5 mL of acetone, respectively) to 10 mL of an aqueous solution of PVA (1%, w/v), under sonication (Branson Sonifier 450, Emerson Electric Co., USA). The microtip of the ultrasonic homogenizer was placed in the aqueous phase, leaving 1 cm distance from the bottom of the vial. To minimize the evaporation of the liquid, an aluminium foil was placed over the opening of the vial. Pulsed mode, with a cycle of 40%, sonication output of 20%, and sonication time of 1 min, avoided foaming and enabled adequate temperature control. The sample vial was surrounded with ice during the sonication process. Acetone was evaporated to obtain an aqueous dispersion of γ-Fe_2O_3/PLGA NPs (Büchi Rotavapor® rotary evaporator, Büchi, Switzerland), and the NPs were then cleaned by repeated magnetic separation from the aqueous medium (0.4 T permanent magnet) and redispersion in water, until the conductivity of the supernatant was $\leq$10 μS cm^{-1}.

Finally, (γ-Fe_2O_3/PLGA)/CS (core/shell)/shell particles (of 4:3 γ-Fe_2O_3/PLGA:CS weight ratio) were obtained by a coacervation method, which was also used to obtain pure CS NPs.[77–79] Initially, 10.5 mg of CS was progressively dissolved in 25 mL of an aqueous solution of acetic acid (2%, v/v) containing 1% (w/v) Kolliphor® P-188, under mechanical stirring (1000 rpm), and 14 mg of γ-Fe_2O_3/PLGA NPs was then homogeneously dispersed in this aqueous phase under mechanical stirring (700 rpm). At that moment, 6.25 mL of 20% (w/v) solution of Na_2SO_4 was added drop-wise (1.25 mL min^{-1}) under sonication (cycle of 50%, sonication output of 20%, and sonication time of 15 min) to obtain the aqueous dispersion of (core/shell)/shell particles. The (γ-Fe_2O_3/PLGA)/CS NPs were cleaned repeatedly by magnetic separation and redispersion in water until the conductivity of the supernatant was $\leq$10 μS cm^{-1}. In contrast, cleaning of the pure CS particles was achieved by repeated cycles of centrifugation (30 min at 9500 rpm, Centrikon T-124 high speed centrifuge, Kontron, France) and redispersion in water, until the conductivity of the supernatant was $\leq$10 μS cm^{-1}.

All experiments were carried out in triplicate ($n = 3$), and the particle production performance (yield, %) was determined by using eqn (1):

$$\text{Yield (\%)} = \frac{\text{amount of NPs obtained (mg)}}{\text{summation of materials used in the preparation of these NPs (mg)}} \times 100 \qquad (1)$$

This journal is © The Royal Society of Chemistry 2021

J. Mater. Chem. B, 2021, **9**, 4963–4980 | **4965**

Characterization

Particle size, size distribution (polydispersity index, PdI), and zeta potential (ζ) were determined after dilution of the colloids in water ($\approx 0.1\%$, w/v) (n = 3) (Zetasizer Nano-ZS, Malvern Instruments Ltd., UK). The cell temperature was $25.0 \pm 0.5\ ^\circ$C, and the detection angle was 60°.

High resolution transmission electron microscopy (HRTEM), high-angle annular dark field scanning transmission electron microscopy (HAADF-STEM), and annular bright field scanning transmission electron microscopy (ABF-STEM) (Titan G2 60-300 FEI microscope, Thermofisher Scientific Inc., USA; operating at an accelerating voltage of 300 kV) helped in visualizing the nanostructures and in evaluating the complete coating of the cores by the polymeric matrices. Drops of the dilute aqueous NP dispersions ($\approx 0.1\%$, w/v) were poured on formvar/carbon-coated copper microgrids and dried in a convection oven ($25.0 \pm 0.5\ ^\circ$C, 24 h) (J. P. Selecta, S. A., Spain). Elemental analysis was performed during the TEM measurements by using an energy dispersive X-ray (EDX) spectrometer (Bruker Nano GmbH, Germany).

Short-term colloidal stability at $4.0 \pm 0.5\ ^\circ$C was tested in water (n = 3). The aqueous dispersion of (core/shell)/shell NPs (1 mg mL^{-1}, pH $\approx$ 6) was stored at this temperature, and the evolution of size, PdI and ζ values of the particles was measured as a function of time following storage. These are parameters that are considered as benchmarks for characterizing the stability of colloidal systems.[29] At each sampling time a formulation was tested and not returned to the storage conditions.

CS coating onto the (γ-Fe$_2$O$_3$/PLGA) particles was qualitatively evaluated by determining the influence of pH (pH values from 3 to 9, in the presence of 10^{-3} M KNO$_3$) on the ζ values of these NPs. Determinations were done at room temperature (n = 12), after 24 h of contact under mechanical stirring (200 rpm, Boeco universal orbital shaker OS-10, Boeco, Germany).

Mineralogical purity and crystallinity of iron oxide-based NPs are important factors that contribute to their magnetic responsiveness.[29,80,81] In view of this, characterization of the internal structure of the γ-Fe$_2$O$_3$ nuclei and the (γ-Fe$_2$O$_3$/PLGA) and (γ-Fe$_2$O$_3$/PLGA)/CS particles was done by X-ray diffractometry (Philips PW1710 diffractometer, The Netherlands), using the Debye–Scherrer method with Cu-Kα radiation of λ = 1.5405 Å.

The magnetic characteristics of the (core/shell) and (core/shell)/shell NPs were determined at $25.0 \pm 0.5\ ^\circ$C, under the influence of a magnetic field ranging from -4000 to 4000 kA m^{-1} (Manics DSM-8 vibrating magnetometer, France). Additionally, the magnetic field responsive behaviour of a 0.1% (w/v) aqueous NP dispersion was qualitatively analysed by optical microscope visualization of the colloid under exposure to a 0.4 T permanent magnet (Olympus BX40F4 microscope, Olympus Optical Co. Ltd, Japan). A Gilmont (USA) micrometer syringe was used to deposit gently one droplet (≈ 10 µL) of the colloid on a dry and clean microscope glass slide. The magnet was situated at a distance of 3 cm from the centre of the droplet, and images were then captured with a video camera at t = 5 s.

Iron concentration was determined by inductively coupled plasma-high resolution mass spectrometry (ICP-HRMS, Element

XR High Resolution ICP-MS system, ThermoFisher Scientific Inc., USA).[82] Prior to analysis, the (γ-Fe$_2$O$_3$/PLGA) particles and (γ-Fe$_2$O$_3$/PLGA)/CS particles were disintegrated by adding 2.5 mL of aqua regia (3 : 1 HNO$_3$: HCl molar ratio) to 25 µL of 0.1% (w/v) aqueous NP dispersion. After 12 h of contact, water was added to the volumetric flask (final volume: 25 mL) and the sample was analysed.

Longitudinal (r_1) and transversal (r_2) relaxivities of (core/shell) NPs and (core/shell)/shell NPs were determined *in vitro* at a low magnetic field (1.44 T) and $37.0 \pm 0.5\ ^\circ$C (Bruker Minispec MQ-60 spectrometer, Bruker BioSpin, Germany),[83] using iron concentrations ranging from 0.25 to 2.00 mM. Transverse (or spin–spin) relaxation time (T_2) values were measured by using the standard Carr–Purcell–Meiboom–Gill (CPMG) pulse sequence, while the longitudinal (or spin–lattice) relaxation time (T_1) was measured using the standard inversion-recovery pulse sequence.

Haemocompatibility

Interaction of (γ-Fe$_2$O$_3$/PLGA) NPs and (γ-Fe$_2$O$_3$/PLGA)/CS NPs with blood components was evaluated to postulate their possibilities for clinical applications, *i.e.* magnet-guided chemotherapy plus hyperthermia. The methodology has been detailed previously,[21,39,84,85] being appropriate in the evaluation of nanoformulations. In brief, blood samples were obtained from two healthy female adults (24 and 45 year old), and poured into flasks containing EDTA (prior to haemolysis, and platelet activation assays) or NaH$_2$(C$_3$H$_5$O (COO)$_3$) (prior to complement system activation, and plasma clotting time experiments). The colloids were kept in contact with blood aliquots to evaluate their impact on erythrocytes, coagulation, and the complement system (n = 3). PBS was used as a negative control. A validated ultraviolet-visible (UV-Vis) spectrophotometric method was used in the study.

In vitro proliferation studies

HFF-1 human foreskin fibroblasts were cultured in DMEM supplemented with 2 mM L-glutamine, 10% FBS and 1% penicillin–streptomycin, at $37.0 \pm 0.5\ ^\circ$C in a humidified atmosphere of 5% CO$_2$ [MCO-19AIC(UV) CO$_2$ incubator, Sanyo, Japan]. Then, the cells in the exponential growth phase were seeded into 96-well plates (10^4 cells per well) and were pre-incubated for 24 h ($37.0 \pm 0.5\ ^\circ$C, 5% CO$_2$), and the medium in the wells was replaced with fresh medium containing γ-Fe$_2$O$_3$/PLGA or (γ-Fe$_2$O$_3$/PLGA)/CS particles (0.1 to 100 µg mL^{-1} of iron concentration).

Following the ISO-10993-5 standard,[86] cell viability was tested (in quadruplicate) by the MTT proliferation assay, by determining mitochondrial dehydrogenase activity. After 24 h of contact, 200 µL of MTT solution in cell culture medium (0.5 mg mL^{-1}) was added to each well. After incubation for 2 h at $37.0 \pm 0.5\ ^\circ$C and 5% CO$_2$, the culture medium was removed and the resultant formazan crystals were solubilized with 200 µL of DMSO. The absorbance of converted dye, which is proportional to the number of viable cells (metabolically active cells), was measured at 550 nm using a Dynatech MR7000

4966 | *J. Mater. Chem. B*, 2021, **9**, 4963–4980

This journal is © The Royal Society of Chemistry 2021

microplate reader (Dynatech Laboratories, Inc., USA). Triton$^®$ X-100 (1%, v/v) was added to the positive control wells. Relative cell viability (RCV, %) and the error related to control wells containing cell culture medium without NPs were calculated by eqn (2) and (3), respectively:

$$\text{RCV (\%)} = \frac{A_\text{test} - A_\text{positive controls for the NPs}}{A_\text{negative controls for the NPs} - A_\text{positive controls for the NPs}} \times 100 \tag{2}$$

$$\text{Error (\%)} = \text{RCV}_\text{test} \times \sqrt{\left(\frac{\sigma_\text{test}}{A_\text{test}}\right)^2 + \left(\frac{\sigma_\text{control}}{A_\text{control}}\right)^2} \tag{3}$$

where A is the absorbance and σ is the standard deviation (SD).

HFF-1 cells were also cultured, similarly as described above, for the cell morphology studies, in quintuplicate. After 24 h of contact with the γ-Fe$_2$O$_3$/PLGA or (γ-Fe$_2$O$_3$/PLGA)/CS particles (0.1 to 100 μg mL^{-1} of iron concentration), Triton$^®$ X-100 (1%, v/v) was added to the positive control wells. After 15 min, all the wells were stained with DAPI (dilution 1 : 3000) to label the cell nucleus and with TO-PRO$^®$-3 iodide (dilution 1 : 1000) to label only dead cells. 10 random image fields captured per well were analysed (20× long working distance, numerical aperture 0.45, air objective lens; Operetta$^®$ High Content Imaging System, PerkinElmer, Inc., USA) being taken for each field fluorescence image for DAPI and TO-PRO$^®$-3 iodide, plus a bright field image. Cell mortality (%) was calculated automatically by Operetta$^®$ Harmony software (PerkinElmer, Inc., USA), whereby live or dead nuclei were identified from the DAPI staining. Dead cells (%) were then determined by the number of nuclei presenting also high levels of TO-PRO$^®$-3 iodide staining.

Magnetic fluid hyperthermia experiments

The *in vitro* heating behaviour of an aqueous dispersion of (γ-Fe$_2$O$_3$/PLGA)/CS NPs (10 mg mL^{-1}, 5 mL) compared to a control formulation (*i.e.* aqueous medium without particles) was investigated at 25.0 ± 0.5 °C (n = 3). To that aim, a high frequency alternating electromagnetic field induced by a power supply equipped with a solenoid was used (diameter: 20 mm; length: 100 mm; number of spirals: 70). Magnetic field frequency and intensity values were 250 kHz and 4 kA m^{-1}, respectively, which were within the average commonly fixed to do such characterization[37,39,49,87] and below the human tolerance threshold.[88] Temperature data were continuously logged using a fiber optic thermometry unit connected to a laptop computer.

The antitumour magnetic hyperthermia activity of the (γ-Fe$_2$O$_3$/PLGA)/CS NPs was evaluated on the T-84 colonic adenocarcinoma cell line (American Type Culture Collection, USA). Detailed description of the procedure can be found in the literature.[39,89,90] Briefly, cells were seeded into 24-well plates (10^4 cells per well) and incubated for 2 h in the presence (or absence) of the NPs (0.4%, w/w) (37.0 ± 0.5 °C, 5% CO$_2$). Then, cell suspensions were centrifuged (10 min at 4000 rpm) to separate the cells from the unbound or weakly bound magnetic nanocomposites, and the cell pellets were re-suspended in 200 μL

of culture medium. The oscillating electromagnetic gradient was then applied (or not) to the cell suspensions for 1 h, and the cells were incubated at room temperature for 30 min and then washed twice in PBS and suspended in the culture medium. Finally, the cells were seeded into 24-well plates (10^4 cells per well) and kept under culture conditions for 48 h (37.0 ± 0.5 °C, 5% CO$_2$). Finally, cell viability was evaluated by the MTT-based colorimetric assay.

In vivo MRI studies

All the *in vivo* experiments were done in the BIONAND Animal Experimentation Service. They were approved by the local Animal Care Committee and performed in compliance with the EU Directive 2010/63/EU (2010) and the Spanish legislation for the care and use of laboratory animals (R.D. 53/2013).

Male Balb/c mice, 22 g in weight (Janvier Labs, France), were anesthetized with 1% isoflurane, and their tail veins were cannulated. Then, the mice were introduced in the MRI system. Respiratory signals and body temperature were monitored throughout the MRI experiment. The (γ-Fe$_2$O$_3$/PLGA) or (γ-Fe$_2$O$_3$/PLGA)/CS NPs were intravenously injected at an iron concentration of 5 mg kg^{-1}. The study was performed in triplicate on a Bruker BioSpec$^®$ 9.4 T animal MRI system (BioSpec 94/20 USR superconducting magnet system, Bruker BioSpin, Germany) equipped with a 400 mT m^{-1} gradient and a 40 mm quadrature bird-cage resonator.

High resolution T_2-weighted images were acquired using a turbo-RARE sequence with respiratory gating (echo time, TE: 16 ms; repetition time, TR: 1000 ms; averages: 4; in-plane resolution: 156 μm; and slice thickness: 1 mm). Quantitative T_2 measurements were performed using a multi-echo spin echo sequence (TE ranging from 7 to 448 ms, TR: 3500 ms, field of view: 4 cm, matrix size: 128 × 128, and slice thickness: 1 mm). Time-courses were followed by using a turbo-RARE sequence with the parameters indicated above, except for only one average to improve temporal resolution (one image every 30 s). The acquisition scheme was as follows: T_2-weighted, quantitative T_2 map, intravenous injection of the NPs, time-course for 35 min, T_2-weighted, and quantitative T_2 map. The first 35 min time-courses were analysed semi-quantitatively using eqn (4):

$$\text{RE (\%)} = \frac{I_t - I_\text{o}}{I_\text{o}} \times 100 \tag{4}$$

where RE is the modulus of relative signal enhancement, I_t is the signal intensity at any given time after injection of NPs, and I_0 is the signal intensity before injection.

Biodistribution was characterized by quantitative T_2 mapping at 0, 1, and 24 h. Average T_2 values were calculated within different regions of interest placed on the liver, spleen, kidneys, and muscle, as previously described.[91,92]

Ex vivo histology evaluation of iron deposits and toxicity assessment

Histology was determined by conventional optical microscopy visualization of tissue samples, at 24 h post-intravenous injection of (γ-Fe$_2$O$_3$/PLGA) and (γ-Fe$_2$O$_3$/PLGA)/CS NPs. Mice were sacrificed and the liver, kidney, spleen, lung and heart were

This journal is © The Royal Society of Chemistry 2021

J. Mater. Chem. B, 2021, **9**, 4963–4980 | **4967**

extracted. Tissues were fixed in 4% (w/v) aqueous CH_2O solution (buffered to pH 7.0 ± 0.5) for 48 h, changing this liquid medium after 24 h. Then, the tissue samples were dehydrated with EtOH and soaked in paraffin (at 56.0 ± 0.5 °C for 2 h, under mechanical stirring) (LEICA TP 1020 Semi-enclosed Benchtop Tissue Processor, Leica Biosystems Nussloch GmbH, Germany). Finally, the samples were embedded in paraffin (Leica EG1150 Modular Tissue Embedding Center, Leica Biosystems Nussloch GmbH, Germany), and then cut into 7 μm-sized sections using a microtome blade (Thermo Scientific™ HM 360 microtome, ThermoFisher Scientific Inc., USA).

Tissue samples were stained with Prussian blue (PB) to visualize iron deposits. To that aim, the tissue slides were deparaffinized, rehydrated, and immersed for 30 min in a freshly prepared mixture of equal parts of 20% (v/v) HCl and 10% (w/v) $K_4[Fe(CN)_6]$ solution. The tissue sections were then washed thrice in water and counter stained with nuclear fast red for 5 min. Finally, the sections were rinsed twice with distilled water, EtOH 100%, followed by 100% xylene, and mounted with coverslips for observation under an optical microscope.

Tissue samples were also stained with haematoxylin and eosin (H&E) to assess tissue architecture. Deparaffinization and rehydration of the tissue slides were done before staining with H&E. Staining was possible by immersion of the samples for 5 min in H, washing twice in water, and immersion of the tissue samples in E for 2 min. The slides were then dehydrated in ascending grades of EtOH (from 70 to 100%), cleared in 100% xylene, and mounted using glass coverslips for observation under a microscope.

Statistical analysis

Statistical analyses were done using the IBM SPSS Statistics software package (version 26.0; IBM Corporation, USA). Experimental data were expressed as mean value ± SD. Student's t-test or two-way analysis of variance helped to compare results considering 95% confidence interval. Differences were considered statistically significant at $p < 0.05$.

Results and discussion

Characterization

The *in vivo* fate and use of magnetic colloids in biomedicine is considerably defined by their size and surface electric charge, among other relevant characteristics. Such properties can be tailored when engineering the iron oxide-based particles to prevent capture by the MPS.[7,29] This may further facilitate reaching the malignant tissue by passing through the gap junction between endothelial cells of the leaky tumour vasculature (up to ≈600 nm).[93,94]

The mean size (and PdI) of γ-Fe_2O_3 nuclei, pure CS particles, and (γ-Fe_2O_3/PLGA) NPs was determined by photon correlation spectroscopy (PCS), and was found to be 9.1 ± 3.2, 353.4 ± 20.6, and 285.3 ± 4.2 nm, respectively. The formulation of (γ-Fe_2O_3/PLGA)/CS (core/shell)/shell NPs (of 4:3 γ-Fe_2O_3/PLGA:CS

weight ratio) by coacervation reported adequate particle production performances (≈45%), and appropriate size (325.8 ± 8.5 nm, compatible with parenteral administration) and ζ values (23.3 ± 0.4 mV). The stealth coating and positive surface electric charge provided by CS to the γ-Fe_2O_3/PLGA nanostructure are expected to prevent the premature clearance of the (core/shell)/shell NPs from the systemic circulation,[52–55] thus favouring appropriate plasma half-lives to reach the tumour site and provide clinically relevant concentrations of any given therapeutic agent. Furthermore, these positive ζ values may facilitate NP internalization by negatively charged cancer cells, thus possibly assuring the deep contact of the therapeutic molecule with intracellular targets.[55,61–64,95,96]

The results from short-term stability studies are compiled in Table 1. From the results, it could be hypothesized that the preparation technique may be used in the formulation of appropriately stabilized (core/shell)/shell NPs. In fact, no NP aggregation was observed, and no appreciable change in the size and surface electric charge of the nanocomposites was detected by PCS after 1 month of storage at 4.0 ± 0.5 °C in water (Table 1).

HRTEM, HAADF-STEM, and ABF-STEM photographs ratified that the iron oxide nuclei were embedded in the polymeric matrices (Fig. 1a–d), while the EDX Fe and N element mappings of these (core/shell)/shell particles demonstrated the homogeneous distribution of γ-Fe_2O_3 nuclei within the NP matrix (Fig. 1e) and the coating of CS onto the γ-Fe_2O_3/PLGA nanostructure (Fig. 1f). Aggregation of NPs observed in the figure was associated with the method of sample preparation (drying) for electron microscopy observations.[38,49,97,98]

EDX analyses also revealed the existence of the elements Fe, C, N, and O for the NPs (Fig. 1g). The Fe and N elements arise from the γ-Fe_2O_3 cores and CS shell, respectively. These observations, combined with data from the electrokinetic characterization of the particles (see Fig. 2a), qualitatively confirmed the formation of the (γ-Fe_2O_3/PLGA)/CS (core/shell)/shell nanostructure. Finally, the use of copper-based grids for EM characterization contributed to the appearance of the Cu element in this analysis,[38] while the presence of Si in the EDX spectra in such a dilute NP sample could be due to the generation of secondary fluorescence by the fluorescence detector.[99]

Table 1 Evolution of size (nm), polydispersity index (PdI) and zeta potential (ζ, mV) of (γ-Fe_2O_3/PLGA)/CS particles as a function of time. The aqueous dispersion of NPs (1 mg mL^{-1}, pH ≈ 6) was stored at 4.0 ± 0.5 °C. Experimental data are expressed as means ± SDs of triplicate experiments (n = 3)

Time (days)	Size (nm)	PdI	ζ (mV)
0	325.8 ± 8.5	0.367 ± 0.007	23.3 ± 0.4
1	325.8 ± 10.5	0.439 ± 0.070	16.9 ± 0.8
3	332.3 ± 11.3	0.358 ± 0.049	32.8 ± 0.7
5	336.3 ± 2.4	0.335 ± 0.043	20.1 ± 0.4
7	330.2 ± 3.9	0.360 ± 0.047	23.5 ± 0.4
10	333.9 ± 6.4	0.302 ± 0.029	24.0 ± 0.7
14	316.7 ± 13.0	0.291 ± 0.043	12.4 ± 2.6
18	322.6 ± 8.4	0.317 ± 0.006	22.4 ± 0.7
22	337.9 ± 4.2	0.360 ± 0.004	25.9 ± 0.6
30	323.8 ± 30.2	0.377 ± 0.084	25.9 ± 0.6

4968 | *J. Mater. Chem. B*, 2021, **9**, 4963–4980

This journal is © The Royal Society of Chemistry 2021
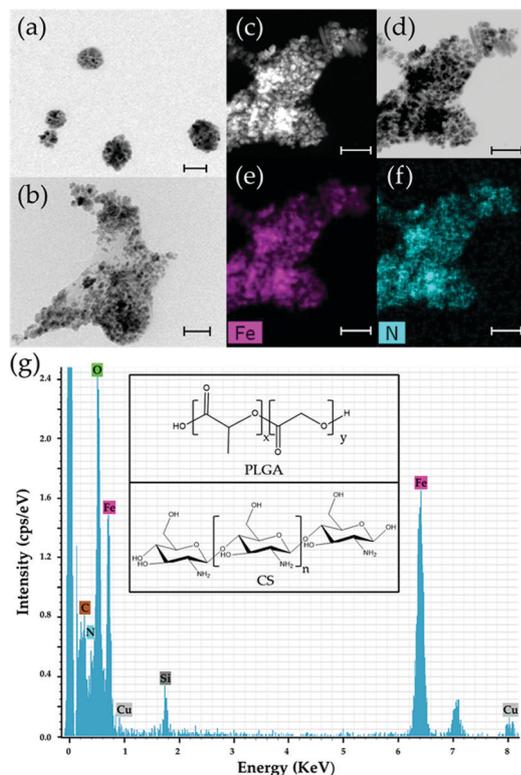
Fig. 1 (a) HRTEM of the (γ-Fe$_2$O$_3$/PLGA) (core/shell) particles. (b) HRTEM, (c) HAADF-STEM, and (d) ABF-STEM images of the (γ-Fe$_2$O$_3$/PLGA)/CS nanocomposites; EDX mapping analysis of the (e) Fe and (f) N elements of the sample in (c and d); and (g) EDX spectra of the (core/shell)/shell NPs. Inset: Chemical structures of PLGA and CS. Bar lengths: 300 nm (a) and 100 nm (b, c, d, e, and f).

Fig. 2 (a) Zeta potential (ζ, mV) of (■) γ-Fe$_2$O$_3$/PLGA NPs, (▲) CS NPs, and (□) (γ-Fe$_2$O$_3$/PLGA)/CS NPs as a function of pH in the presence of 1 mM KNO$_3$. Data are presented as mean value $\pm$ SD (n = 9). Lines are a guide to the eye and have no other significance. (b) American Society for Testing and Materials (ASTM) pattern for γ-Fe$_2$O$_3$. X-ray diffractograms of (c) γ-Fe$_2$O$_3$, (d) (γ-Fe$_2$O$_3$/PLGA), and (e) (γ-Fe$_2$O$_3$/PLGA)/CS particles. The intensity is expressed in arbitrary units (a. u.).

Given the different electrokinetic properties of PLGA-based[41] and CS-based particles,[37] electrophoresis was used to confirm qualitatively the coating efficiency of CS around the (γ-Fe$_2$O$_3$/PLGA) particles. The study was focused on the effect of pH on the surface electric charge (ζ values) of the particles in the presence of 10^{-3} M KNO (Fig. 2a). The negative surface charge of these γ-Fe$_2$O$_3$/PLGA particles may come from ionized weak acid groups, probably carboxylic-end groups.[41,100] Under the experimental conditions, the decrease in absolute ζ values as pH became more acidic was associated to the neutralization of the negative regions of the polymer by adsorption of increasing amounts of H$^+$. On the opposite, the increasingly negative ζ values may come from the increase in OH$^-$ ions in the dispersion media, which could tend to favour a gain in H$^+$. In contrast, CS particles were characterized by positive ζ values for the whole pH range. The residual amino groups of CS could be responsible for this positive electric charge at the polymer–solution interface,[37,101] despite the use of SO$_4^{2-}$ as a precipitant and regardless of the negative groups of the stabilizer Kolliphor® P-188 which could persist on the particle surface even after cleaning. Finally, Fig. 2a further demonstrates that the ζ-pH trends of the (γ-Fe$_2$O$_3$/PLGA)/CS NPs were dominated by the CS shell. This should be the result of the effective CS coating of (γ-Fe$_2$O$_3$/PLGA) particles, leading to a (core/shell)/shell nanostructure
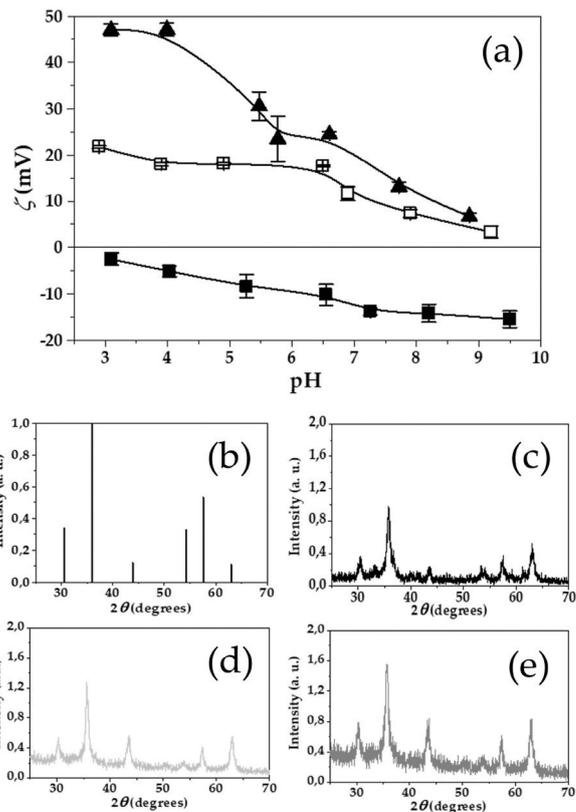
which, from an electrokinetic point of view, is qualitatively similar to the CS particles.

Taking into account the data from the electrophoretic study, the mechanism of formation of the (γ-Fe$_2$O$_3$/PLGA)/CS (core/shell)/shell particles could be hypothesized. Attractive electrostatic interactions may take place under the acid condition characteristics of the aqueous medium where the nanocomposites were formed (pH $\approx$ 3.3).[56,57] These interactions are expected to occur between the negatively charged γ-Fe$_2$O$_3$/PLGA particles and the positively charged CS matrix at this pH (see Fig. 2a), favouring the accumulation of CS onto the γ-Fe$_2$O$_3$/PLGA surface, and thus resulting in the formation of a (γ-Fe$_2$O$_3$/PLGA)/CS nanostructure.

Fig. 2b presents the American Society for Testing and Materials (ASTM) pattern of γ-Fe$_2$O$_3$ (ASTM No. 24-81). The X-ray diffraction patterns of γ-Fe$_2$O$_3$ (Fig. 2c), (γ-Fe$_2$O$_3$/PLGA) (Fig. 2d), and (γ-Fe$_2$O$_3$/PLGA)/CS (Fig. 2e) particles coincided well with this pattern. This could be an indication of the mineralogical purity and high crystalline nature of the synthesized γ-Fe$_2$O$_3$ particles (responsible for the superparamagnetic behaviour and adequate responsiveness to magnetic fields),[29] even upon complete coating by both the PLGA and CS matrices.

This journal is © The Royal Society of Chemistry 2021

J. Mater. Chem. B, 2021, **9**, 4963–4980 | **4969**

2θ values of the γ-Fe$_2$O$_3$ nuclei embedded in the (core/shell)/shell NPs were 30.30°, 35.64°, 43.66°, 54.10°, 57.36°, and 63.04°, and they could be assigned to the (220), (311), (400), (422), (511), and (440) planes of these iron oxide particles, respectively.[102–104]

Magnetic responsiveness

The hysteresis cycle of the γ-Fe$_2$O$_3$/PLGA and (γ-Fe$_2$O$_3$/PLGA)/CS NPs, plotted in Fig. 3a, characterized their field responsive behaviour. These particles apparently exhibited a soft magnetic character, given that the increasing and decreasing field ramps of the cycle were hardly discernible with the sensitivity of the instrument used. From the linear portions (low field) of the curves the initial susceptibility was calculated to be $\chi_i = (0.071 \pm 0.009) \times 10^{-3}$ [and $(0.102 \pm 0.013) \times 10^{-3}$] m^3 kg^{-1} and the saturation magnetization was 4.98 ± 0.41 (and 7.18 ± 0.59) Am^2 kg^{-1} for the (core/shell)/shell (and core/shell) NPs. The magnetic behaviour of the (γ-Fe$_2$O$_3$/PLGA)/CS particles was quite similar to that of the γFe$_2$O$_3$/PLGA particles, except that the CS shell reduced slightly the magnetization of the (core/shell)/shell sample. This could be the consequence, at equal mass of the sample analysed, of the smaller amount of γ-Fe$_2$O$_3$ nanocores contained inside the (γ-Fe$_2$O$_3$/PLGA)/CS NPs in comparison to the sample of γ-Fe$_2$O$_3$/PLGA particles.

In any case, the appropriate magnetic responsive behaviour of the (core/shell)/shell NPs was further qualitatively confirmed by optical microscope visualization of the colloid under exposure to a permanent magnet (Fig. 3b). The initially homogeneous aqueous dispersion of (core/shell)/shell particles changed markedly, and the formation of chainlike aggregates parallel to the field lines occurred. This could result from the notable contribution of the magnetic interaction over the DLVO colloidal interactions between the NPs (*e.g.* electrostatic van der Waals and hydration or acid–base). However, *in vivo* experiments should be done to clarify if this magnetic responsiveness could determine the accumulation of the (γ-Fe$_2$O$_3$/PLGA)/CS particles at a targeted site.

Finally, a preliminary study on the potential use of the nanocomposites as MRI contrast agents was accomplished *in vitro*. r_1 and r_2 values for the γ-Fe$_2$O$_3$/PLGA particles were found to be 0.2 and 48.5 mM^{-1} × s^{-1} (Fig. 4a), respectively, whereas 0.4 and 61.4 mM^{-1} × s^{-1} were the r_1 and r_2 values for the (γ-Fe$_2$O$_3$/PLGA)/CS nanocomposites (Fig. 4b), respectively. These relaxivities are comparable to those reported previously for similar iron oxide-based nanostructures[77] and iron oxide-based MRI contrast agents, *e.g.* Sinerem® or Ferumoxytol.[105–107] The r_2/r_1 ratios for γ-Fe$_2$O$_3$/PLGA and (γ-Fe$_2$O$_3$/PLGA)/CS were 243.5 and 153.5, respectively, suggesting the potential application of these NPs as T_2 contrast agents.[108,109]

In vitro haemocompatibility and cytotoxicity

The contact of nanoparticulate systems with blood components may lead to adverse effects, *e.g.*, platelet and complement system
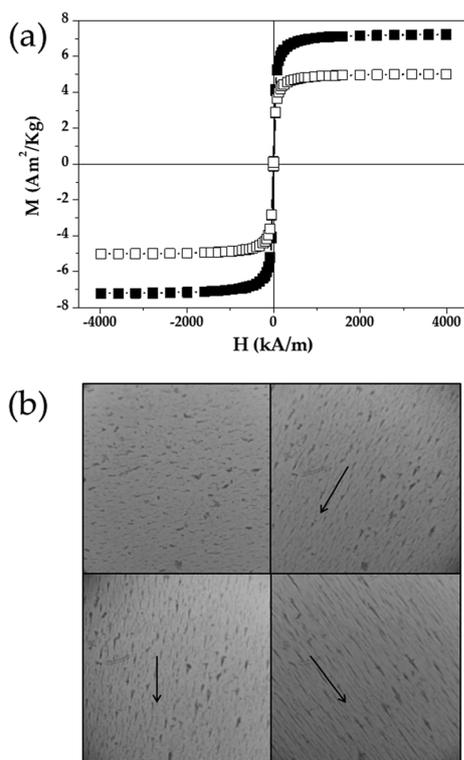

Fig. 3 (a) Hysteresis cycles of the γ-Fe$_2$O$_3$/PLGA (■) and (γ-Fe$_2$O$_3$/PLGA)/CS (□) particles; and (b) optical microphotographs (magnification 20×) of the (core/shell)/shell colloid (0.1%, w/v) under the influence of a 0.4 T permanent magnet (in the direction of the arrow).
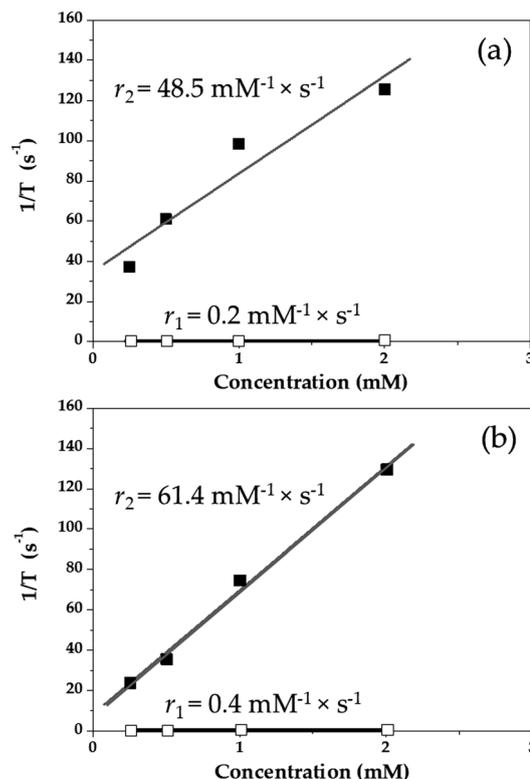

Fig. 4 Longitudinal (□, $1/T_1$, s^{-1}) and transverse (■, $1/T_2$, s^{-1}) relaxation rates as a function of the iron concentration (mM) in (a) γ-Fe$_2$O$_3$/PLGA and (b) (γ-Fe$_2$O$_3$/PLGA)/CS NPs, measured at 1.44 T.

4970 | *J. Mater. Chem. B*, 2021, **9**, 4963–4980

This journal is © The Royal Society of Chemistry 2021

Table 2 *In vitro* blood compatibility of the γ-Fe$_2$O$_3$/PLGA and (γ-Fe$_2$O$_3$/PLGA)/CS particles: haemolysis (%), platelet activation (sP-selectin release, ng mL^{-1}), complement activation (C3a release: C3a desArg, ng mL^{-1}), and plasma recalcification time ($T_{1/2\ max}$, min). Experimental data are expressed as means $\pm$ SDs of triplicate experiments ($n = 3$)

Sample	Haemolysis (%)				sP-selectin release (ng mL^{-1})	C3a desArg (ng mL^{-1})	$T_{1/2max}$ (min)
	Incubation time						
	2 h	4 h	8 h	24 h			
γ-Fe$_2$O$_3$/PLGA NPs	2.5 $\pm$ 0.6	2.5 $\pm$ 0.9	2.3 $\pm$ 0.8	2.5 $\pm$ 0.5	110 $\pm$ 8	305 $\pm$ 9	14.2 $\pm$ 1.1
(γ-Fe$_2$O$_3$/PLGA)/CS NPs	2.6 $\pm$ 0.8	2.9 $\pm$ 0.4	2.6 $\pm$ 0.3	2.8 $\pm$ 0.6	114 $\pm$ 8	306 $\pm$ 10	14.3 $\pm$ 0.9
Control (PBS solution)	0	0	0	0	97 $\pm$ 8	295 $\pm$ 7	11.5 $\pm$ 1.7

activation, and lysis of erythrocytes,[29,85] being responsible for (i) thrombotic complications and production of anaphylatoxins, that may activate the immune system;[85] and (ii) haemolytic crisis, that may determine renal damage and anaemia,[85,110] respectively.
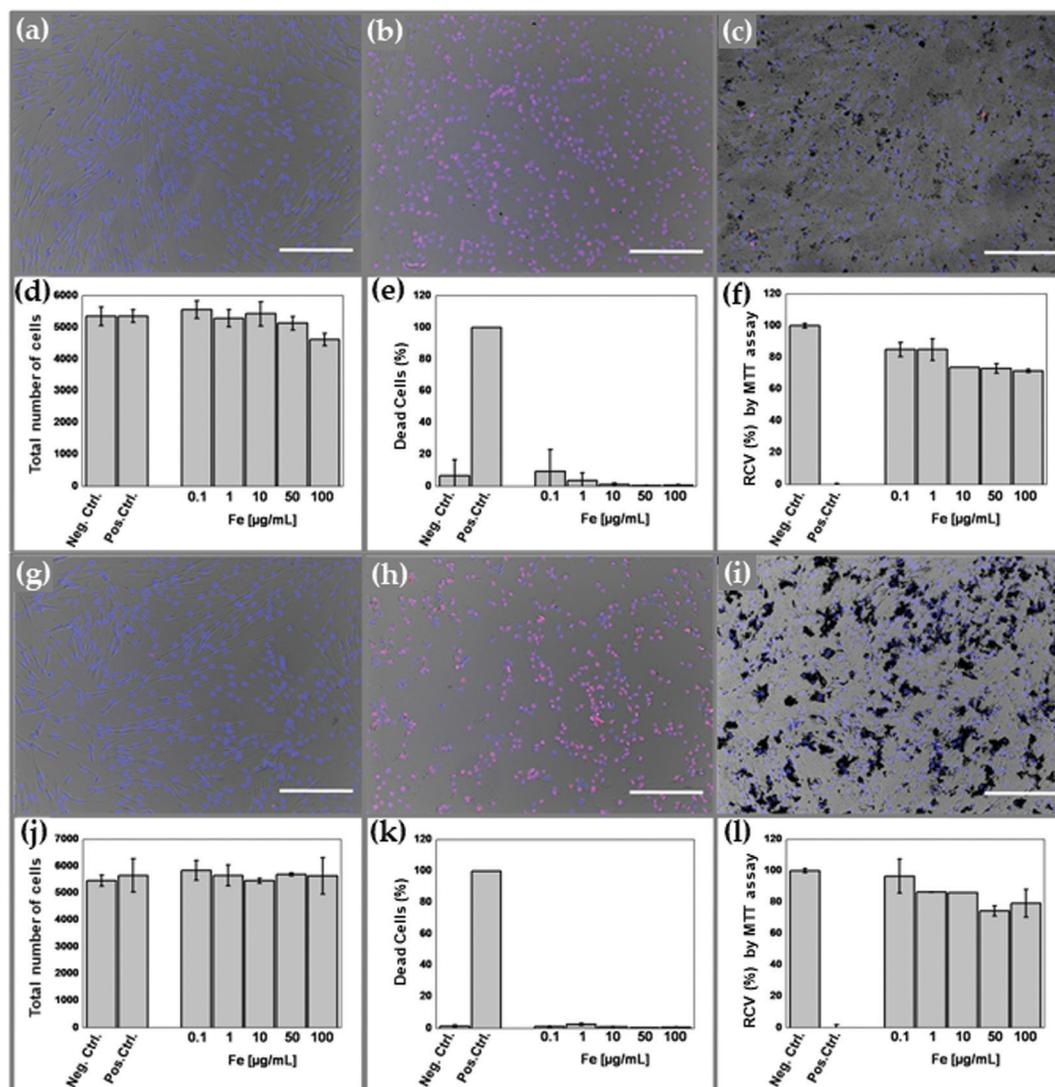

Fig. 5 Representative optical microscopy images of HFF-1 fibroblasts: (a) and (g) are negative controls for the γ-Fe$_2$O$_3$/PLGA and (γ-Fe$_2$O$_3$/PLGA)/CS particles, respectively; (b) and (h) are positive controls for the γ-Fe$_2$O$_3$/PLGA and (γ-Fe$_2$O$_3$/PLGA)/CS NPs, respectively; and HFF-1 cells exposed to (c) γ-Fe$_2$O$_3$/PLGA NPs (100 μg mL^{-1} of iron) or (i) (γ-Fe$_2$O$_3$/PLGA)/CS NPs (100 μg mL^{-1} of iron). These images show the merge of bright field (grey), DAPI (blue) and TO-PRO®-3 iodide (red). Bar lengths: 100 μm. Total number of cells per well (d and j), dead cells (%, e and k), and relative cell viability (RCV, %) by MTT assay (f and l) of HFF-1 fibroblasts, after contact with increasing concentrations (0.1 to 100 μg mL^{-1} of iron) of γ-Fe$_2$O$_3$/PLGA NPs and (γ-Fe$_2$O$_3$/PLGA)/CS NPs, respectively.

Data from *in vitro* blood compatibility tests of γ-Fe$_2$O$_3$/PLGA and (γ-Fe$_2$O$_3$/PLGA)/CS NPs is compiled in Table 2. The null effect on haemolysis (even after 24 h), platelet activation, complement system activation, and plasma clotting time was defined. Therefore, these nanocomposites could be characterized by an appropriate *in vivo* safety margin, being suitable for parenteral administration. Similar results have been obtained in similar iron oxide-based nanosystems.[39–41,87]

The results from the cytotoxic evaluation of γ-Fe$_2$O$_3$/PLGA and (γ-Fe$_2$O$_3$/PLGA)/CS particles in HFF-1 human foreskin fibroblast cells are presented in Fig. 5. It is observed how increasing concentrations, from 0.1 to 100 μg mL^{-1} of iron, of both core/shell and (core/shell)/shell particles induced negligible toxicity in the HFF-1 cell line. In fact, they did not produce significant changes in cell morphology (Fig. 5c and i) and the total number of HFF-1 cells (Fig. 5d and j), at any of the concentrations investigated. Moreover, these NP concentrations did not generate a relevant increase in cell death (Fig. 5e and k). Finally, the RCV (%) of HFF-1 cells remained $\geq$75%, relative to negative controls, at any of the γ-Fe$_2$O$_3$/PLGA (Fig. 5f) and (γ-Fe$_2$O$_3$/PLGA)/CS (Fig. 5l) concentrations analysed. According to ISO-10993-5,[86] these values could be considered as reasonable and non-toxic.

In vitro magnetic fluid hyperthermia

Antitumour magnetic hyperthermia has proven to be more than a promising possibility against cancer.[29,111–113] The heating capability of a (core/shell)/shell aqueous magnetofluid in a high frequency alternating electromagnetic gradient is depicted in Fig. 6a. The (γ-Fe$_2$O$_3$/PLGA)/CS particles transformed into heaters, possibly owing to the oscillation of their magnetic moment and magnetic hysteresis losses.[29,114] As a consequence, the temperature of the magnetofluid rose from 25 °C to the minimum hyperthermia temperature ($\approx$42 °C, in $\approx$32 min). If this temperature is kept constant for $\approx$30 min, it has been described that a tumour mass can be destroyed.[114,115] Then, the maximum temperature reached $\approx$46 °C after $\approx$50 min, and remained at this temperature until the end of the experiment (3 h). Considering these results, an appropriate control over the temperature and heat flux of the magnetofluid could be postulated. This is a prerequisite for hyperthermia, particularly when healthy cells surrounding a solid tumour are damaged when temperature reaches >48 °C.[29,116,117]

Fig. 6b compiles the results from the evaluation of the hyperthermic efficacy of the (γ-Fe$_2$O$_3$/PLGA)/CS NPs against T-84 cells. Experimental data proved that compared to controls the (core/shell)/shell NPs in a high frequency alternating electromagnetic gradient can significantly reduce cell viability (up to $\approx$39%, group *1*) ($p < 0.05$), thus being postulated to be a promising nanotool for antitumour magnetic hyperthermia. Oppositely, when used alone, neither the particles (group *2*) nor the field (group *3*) could be considered of any use against T-84 cells. Finally, *in vivo* magnetic fluid hyperthermia data will help in defining clearly the antitumor effect of the nanostructures.
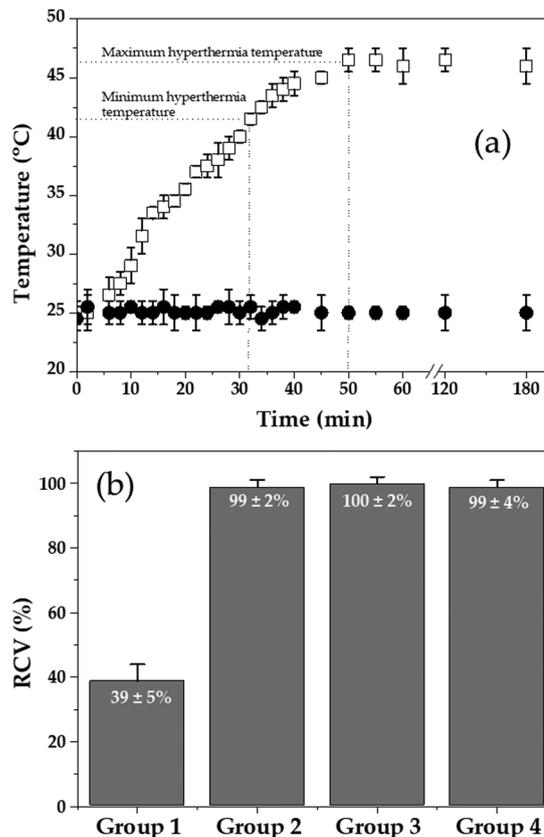

Fig. 6 (a) Heating curve of an aqueous dispersion of (γ-Fe$_2$O$_3$/PLGA)/CS nanocomposites ($\square$, 10 mg mL^{-1}) exposed to a high frequency oscillating electromagnetic gradient (250 kHz, 4 kA m^{-1}), in comparison to data from a control (*i.e.* water, $\bullet$). (b) *In vitro* hyperthermic efficacy of the magnetic (core/shell)/shell NPs on T-84 relative cell viability (RCV, %). Experimental groups are cells incubated in the presence of NPs (0.4%, w/w) with application of the alternating magnetic field (250 kHz, 4 kA m^{-1}) (group 1), or without application of the alternating magnetic field (control group 2); or cells incubated in the absence of NPs with application of the alternating magnetic field (250 kHz, 4 kA m^{-1}) (control group 3), or without application of the alternating magnetic field (control group 4). Experimental data are expressed as means $\pm$ SDs of triplicate experiments (n = 3).

In vivo MRI

Short-term pharmacokinetics of γ-Fe$_2$O$_3$/PLGA (core/shell) NPs after intravenous injection in Balb/c mice was followed by dynamic MRI (Fig. 7). Rapid particle uptake by the liver and spleen was detected (Fig. 7a and b, respectively), with a fast signal increase of $\approx$30% in $\approx$5 min in the liver, whereas in the spleen the increment was slightly more progressive. On the opposite, NP retention by kidneys could be considered almost negligible, given that the initial increase in the relative signal intensity (%) was followed by a fast decrease to baseline (Fig. 7c). No change in the relative signal intensity (%) was observed in muscles. These results suggest rapid recognition of the core/shell particles by the MPS, likely leading to rapid clearance from the bloodstream by Kupffer cells and splenic macrophages.

The *in vivo* fate of the γ-Fe$_2$O$_3$/PLGA NPs was further evaluated qualitatively by T_2-weighted MR images (Fig. 7d–f) and

4972 | *J. Mater. Chem. B*, 2021, **9**, 4963–4980

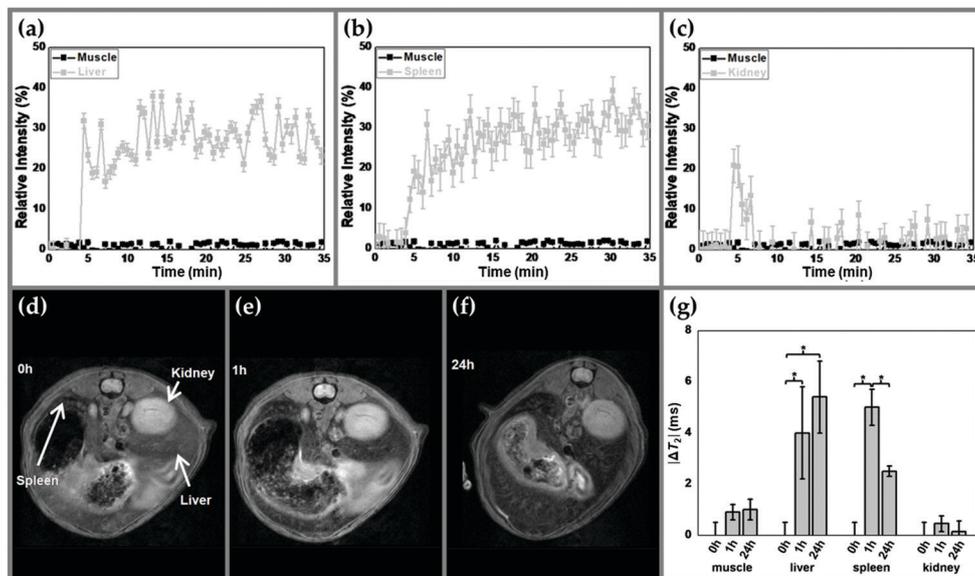This journal is © The Royal Society of Chemistry 2021

Fig. 7 *In vivo* time courses of γ-Fe$_2$O$_3$/PLGA NPs after intravenous injection in Balb/c mice: (a) liver (grey) and muscle (black); (b) spleen (grey) and muscle (black); and (c) kidney (grey) and muscle (black). Representative T_2-weighted MR images of the kidney, spleen, and liver after the injection of the NPs, at the experimental times: (d) 0 h, (e) 1 h, and (f) 24 h. (g) Absolute values of ΔT_2 (ms) as a function of time (hours) of muscle, liver, spleen and kidney after the injection of the core/shell NPs. Experimental data are expressed as means $\pm$ SDs of triplicate experiments (n = 3). The statistical test was significant for data with *($p < 0.05$).

quantitatively by T_2-mapping (Fig. 7g) up to 24 h. Liver and spleen images showed clear hypo-intensity areas at 1 and 24 h postinjection (Fig. 7e and f, respectively). In contrast, significant changes in the kidneys were not observed. Furthermore, a significant decrease in T_2 for the liver ($\Delta T_2 \approx 4$ ms) and spleen ($\Delta T_2 \approx 5$ ms) can be identified in Fig. 7g ($p < 0.05$) at 1 h postinjection. By the end of the study (t = 24 h), the absolute value of ΔT_2 was increased further to ≈ 5.4 ms for the liver

($p < 0.05$), while being partially recovered in the spleen (≈ 2.2 ms, $p < 0.05$). Finally, significant changes in ΔT_2 were not detected in kidneys or muscles during the study.

The biodistribution of the (γ-Fe$_2$O$_3$/PLGA)/CS particles was found to be quite different from what was described for the γ-Fe$_2$O$_3$/PLGA NPs. The uptake of these (core/shell)/shell nanoplatforms by the liver (Fig. 8a) was lower than that observed for the γ-Fe$_2$O$_3$/PLGA particles (Fig. 7a), given that increments in
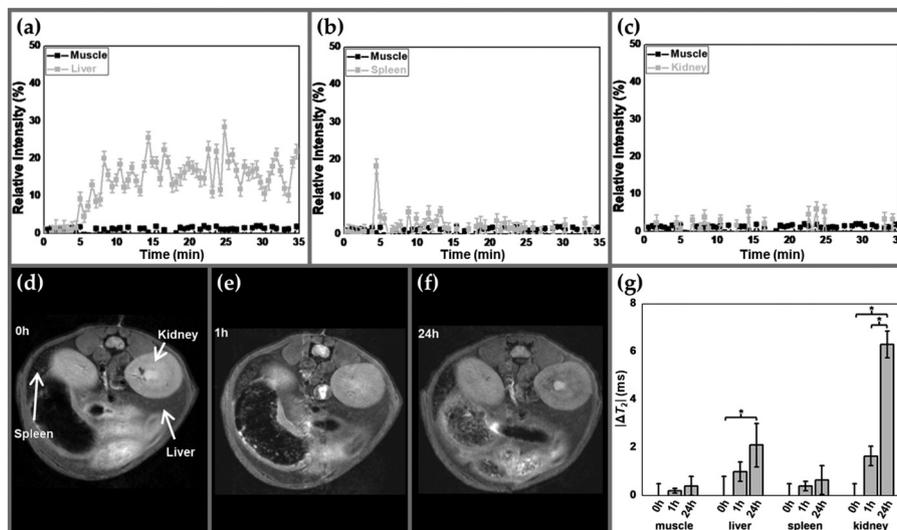

Fig. 8 *In vivo* time courses of (γ-Fe$_2$O$_3$/PLGA)/CS nanocomposites after intravenous injection in Balb/c mice: (a) liver (grey) and muscle (black); (b) spleen (grey) and muscle (black); and (c) kidney (grey) and muscle (black). Representative T_2-weighted MR images of the kidney, spleen, and liver after the injection of the NPs, at the experimental times: (d) 0 h, (e) 1 h, and (f) 24 h. (g) Absolute values of ΔT_2 (ms) as a function of time (hours) of muscle, liver, spleen and kidney after the injection of the (core/shell)/shell NPs. Experimental data are expressed as means $\pm$ SDs of triplicate experiments (n = 3). The statistical test was significant for data with *($p < 0.05$).

This journal is © The Royal Society of Chemistry 2021

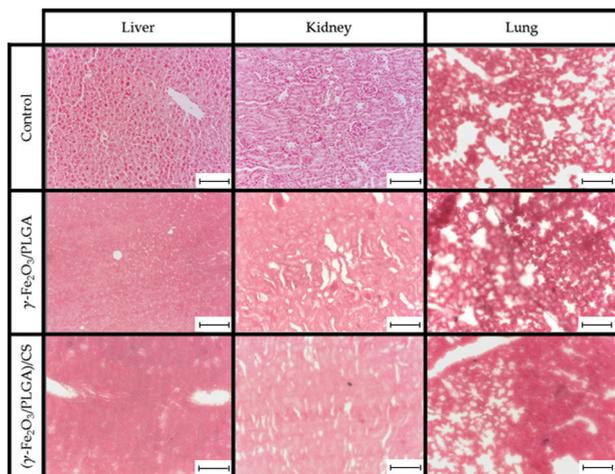*J. Mater. Chem. B*, 2021, **9**, 4963–4980 | **4973**

Fig. 9 PB staining of representative histological sections of control liver, kidney and lung, and liver, kidney and lung at 24 h post-intravenous injection of γ-Fe$_2$O$_3$/PLGA NPs and (γ-Fe$_2$O$_3$/PLGA)/CS nanocomposites. Bar lengths: 100 μm.

the relative signal intensity (%) values were a little smaller, even though the r_2 value of the former was $\approx 30\%$ higher and the amount injected was the same in both cases.

CS coating onto the (core/shell) nanostructure further favoured an almost null uptake of the (γ-Fe$_2$O$_3$/PLGA)/CS NPs by the spleen (Fig. 8b). In view of these results, it could be postulated that CS provided adequate stealth properties to the nanocomposite,[52–55] leading to prolonged blood circulation times (a relevant attribute for biomedical applications). Similarly to γ-Fe$_2$O$_3$/PLGA particles, no change in the relative signal intensity (%) was observed in kidneys and muscles after intravenous injection of the (core/shell)/shell NPs (Fig. 8c).

In vivo distribution data confirmed these findings (Fig. 8d–g). For instance, increments in the absolute value of ΔT_2 for liver induced by the (γ-Fe$_2$O$_3$/PLGA)/CS NPs (up to ≈ 1.9 ms, $p < 0.05$, Fig. 8g)

were found to be smaller than those induced by the γ-Fe$_2$O$_3$/PLGA particles (Fig. 7g). These data may ratify that the uptake of the (core/shell)/shell NPs by the liver was lower than that observed for the γ-Fe$_2$O$_3$/PLGA particles. Quantitative T_2-mapping confirmed the negligible uptake of the (core/shell)/shell nanostructure by the spleen and muscles found in Fig. 8b, which may probably the consequence of an almost null interaction of the particles with splenic macrophages. Finally, significant changes in the absolute value of ΔT_2 were observed for the kidneys ($p < 0.05$), reaching up to ≈ 6.1 ms at 24 h postinjection.

Despite these promising results highlighting the stealthiness of the (γ-Fe$_2$O$_3$/PLGA)/CS NPs, experiments in tumour-bearing mice are needed to better define if magnetically guided targeting can make possible the selective accumulation of the (core/shell)/shell particles in the tumour mass.

Ex vivo histology evaluation of iron deposits and toxicity assessment

PB staining of liver, kidney and lung tissues at 24 h postinjection of γ-Fe$_2$O$_3$/PLGA NPs and (γ-Fe$_2$O$_3$/PLGA)/CS in Balb/c mice is compiled in Fig. 9. Iron deposits in the liver, mainly in Kupffer cells, were observed after administration of the core/shell particles, while iron deposits were not detected in kidneys and lungs. With respect to the (core/shell)/shell nanocomposites, iron deposits were found not only in the liver, but also in kidneys and lungs. All these findings were in agreement with the MRI results (see Fig. 7 and 8). This evaluation may support the hypothesis on the advantageous use of CS if long-circulating properties are intended for a nanoparticulate system.[52–55] In addition, surface modification with CS has been described to favour a more extensive biodistribution, *e.g.* targeting lung tissue.[118]

In order to further evaluate the potential toxicity of γ-Fe$_2$O$_3$/PLGA NPs and (γ-Fe$_2$O$_3$/PLGA)/CS, H&E staining of liver, kidney, spleen, lungs and heart tissues at 24 h postinjection
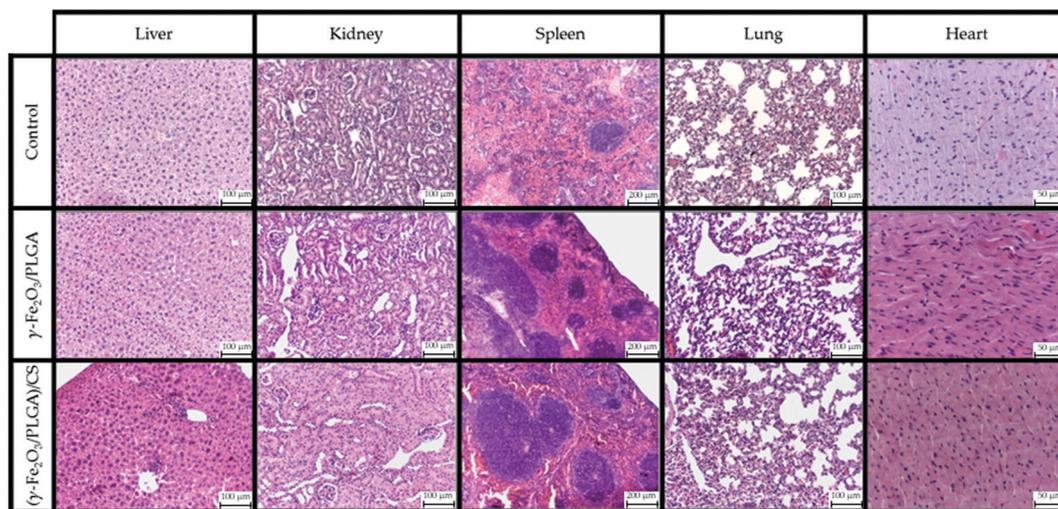

Fig. 10 H&E staining of representative histological sections of control liver, kidney, spleen, lung and heart, and liver, kidney, spleen, lung and heart at 24 h post-intravenous injection of γ-Fe$_2$O$_3$/PLGA NPs and (γ-Fe$_2$O$_3$/PLGA)/CS nanocomposites.

4974 | *J. Mater. Chem. B*, 2021, **9**, 4963–4980

This journal is © The Royal Society of Chemistry 2021

in Balb/c mice was accomplished (Fig. 10). Vacuolated swelling of the cytoplasm of hepatocytes, a common indicator of liver injury, was not found in liver sections. Normal tubular brush borders and glomeruli (including their surrounding Bowman's capsule) were identified in the kidneys. No signs of toxicity were found also in the spleen, lungs, and heart, independently of the type of nanoparticulate system [γ-Fe$_2$O$_3$/PLGA NPs or (γ-Fe$_2$O$_3$/PLGA)/CS particles].

Combining these data with the results coming from the *in vitro* haemocompatibility and cytotoxicity tests (see Section *In vitro haemocompatibility and cytotoxicity*), it could be concluded that the nanocomposites present appropriate biocompatibility and safety for biomedical use.

Conclusions

A methodology has been described for the reproducible formulation of (γ-Fe$_2$O$_3$/PLGA)/CS NPs (≈ 325 nm in size, production performance $\approx 45\%$). This (core/shell)/shell nanostructure was confirmed by electron microscopy and EDX analysis, and by investigation of the electrokinetic properties. Short-term stability (up to one month) was demonstrated by size and surface electric charge determinations. Crystallinity of the γ-Fe$_2$O$_3$ nanocores embedded in the polymer matrix was demonstrated by X-ray diffraction analysis, with this characteristic probably being responsible for the adequate magnetic responsiveness of the nanocomposite (demonstrated *in vitro*). *In vitro* evaluations supported the idea of a potential use of the (γ-Fe$_2$O$_3$/PLGA)/CS particles as T_2 contrast agents and in antitumour magnetic hyperthermia. *Ex vivo* toxicity assessments and *in vitro* blood compatibility and cytotoxicity tests postulated the appropriate biocompatibility and safety of the particles for biomedical use. Finally, *in vivo* MRI studies and *ex vivo* histology determination of iron deposits reinforced the hypothesis on the advantageous use of CS in providing stealth properties to the nanosystem that may help in retarding the recognition by the MPS. Taking together, these biocompatible and long-circulating (core/shell)/shell nanostructures may constitute a potential candidate for theranostic applications (biomedical imaging and hyperthermia) against cancer. Additional experiments in tumour-bearing mice will help in defining if magnetically guided targeting could make possible the selective accumulation of the (core/shell)/shell particles in the tumour mass and the therapeutic effectiveness of this nanoplatform in cancer hyperthermia therapy.

Author contributions

Conceived and designed the experiments: FF-A, CC, MLG-M, JLA. Performed the experiments: FF-A, GG-G, CC. Analysed the data: FF-A, GG-G, CC, JLA. Contributed reagents/materials/analysis tools: MLG-M, JLA. Wrote the paper: FF-A, CC, MLG-M, JLA.

Conflicts of interest

The authors declare that they have no competing interests.

Acknowledgements

Notes and references

1 B. Clares, M. A. Ruiz, V. Gallardo and J. L. Arias, Drug delivery to inflammation based on nanoparticles surface decorated with biomolecules, *Curr. Med. Chem.*, 2012, **19**, 3203–3211.

2 A. Wicki, D. Witzigmann, V. Balasubramanian and J. Huwyler, Nanomedicine in cancer therapy: challenges, opportunities, and clinical applications, *J. Controlled Release*, 2015, **200**, 138–157.

3 M. M. El-Hammadi and J. L. Arias, Nano-sized platforms for vaginal drug delivery, *Curr. Pharm. Des.*, 2015, **21**, 1633–1644.

4 J. Shi, P. W. Kantoff, R. Wooster and O. C. Farokhzad, Cancer nanomedicine: progress, challenges and opportunities, *Nat. Rev. Cancer*, 2017, **17**, 20–37.

5 Z. Li, S. Tan, S. Li, Q. Shen and K. Wang, Cancer drug delivery in the nano era: an overview and perspectives (review), *Oncol. Rep*, 2017, **38**, 611–624.

6 N. Amreddy, A. Babu, R. Muralidharan, J. Panneerselvam, A. Srivastava, R. Ahmed, M. Mehta, A. Munshi and R. Ramesh, Recent advances in nanoparticle-based cancer drug and gene delivery, *Adv. Cancer Res.*, 2018, **137**, 115–170.

7 J. L. Arias, Drug targeting strategies in cancer treatment: an overview, *Mini-Rev. Med. Chem.*, 2011, **11**, 1–17.

8 L. Kotelevets, E. Chastre, D. Desmaële and P. Couvreur, Nanotechnologies for the treatment of colon cancer: from old drugs to new hope, *Int. J. Pharm.*, 2016, **514**, 24–40.

9 Y. Zhang, M. Li, X. Gao, Y. Chen and T. Liu, Nanotechnology in cancer diagnosis: progress, challenges and opportunities, *J. Hematol. Oncol.*, 2019, **12**, 137.

10 B. J. Stephen, S. Suchanti, R. Mishra and A. Singh, Cancer nanotechnology in medicine: a promising approach for cancer detection and diagnosis, *Crit. Rev. Ther. Drug Carrier Syst.*, 2020, **37**, 375–405.

11 A. Sohail, Z. Ahmad, O. A. Bég, S. Arshad and L. Sherin, A review on hyperthermia *via* nanoparticle-mediated therapy, *Bull. Cancer*, 2017, **104**, 452–461.

This journal is © The Royal Society of Chemistry 2021

J. Mater. Chem. B, 2021, **9**, 4963–4980 | 4975

12 J. K. Kang, J. C. Kim, Y. Shin, S. M. Han, W. R. Won, J. Her, J. Y. Park and K. T. Oh, Principles and applications of nanomaterial-based hyperthermia in cancer therapy, *Arch. Pharmacal Res.*, 2020, **43**, 46–57.

13 P. García Calavia, G. Bruce, L. Pérez-García and D. A. Russell, Photosensitiser-gold nanoparticle conjugates for photodynamic therapy of cancer, *Photochem. Photobiol. Sci.*, 2018, **17**, 1534–1552.

14 S. Kwiatkowski, B. Knap, D. Przystupski, J. Saczko, E. Kędzierska, K. Knap-Czop, J. Kotlińska, O. Michel, K. Kotowski and J. Kulbacka, Photodynamic therapy – mechanisms, photosensitizers and combinations, *Biomed. Pharmacother.*, 2018, **106**, 1098–1107.

15 X. Hou, Y. Tao, Y. Pang, X. Li, G. Jiang and Y. Liu, Nanoparticle-based photothermal and photodynamic immunotherapy for tumor treatment, *Int. J. Cancer*, 2018, **143**, 3050–3060.

16 Y. Liu, B. M. Crawford and T. Vo-Dinh, Gold nanoparticles-mediated photothermal therapy and immunotherapy, *Immunotherapy*, 2018, **10**, 1175–1188.

17 M. M. El-Hammadi and J. L. Arias, An update on liposomes in drug delivery: a patent review (2014–2018), *Expert Opin. Ther. Pat.*, 2019, **29**, 891–907.

18 R. Brusini, M. Varna and P. Couvreur, Advanced nanomedicines for the treatment of inflammatory diseases, *Adv. Drug Delivery Rev.*, 2020, **157**, 161–178.

19 A. A. Sebak, B. M. El-Shenawy, S. El-Safy and M. El-Shazly, From passive targeting to personalized nanomedicine: multidimensional insights on nanoparticles' interaction with the tumor microenvironment, *Curr. Pharm. Biotechnol.*, 2020, DOI: 10.2174/1389201021666201211103856.

20 K. R. Gajbhiye, A. Pawar, K. R. Mahadik and V. Gajbhiye, PEGylated nanocarriers: A promising tool for targeted delivery to the brain, *Colloids Surf., B*, 2020, **187**, 110770.

21 M. M. El-Hammadi, A. V. Delgado, C. Melguizo, J. C. Prados and J. L. Arias, Folic acid-decorated and PEGylated PLGA nanoparticles for improving the antitumour activity of 5-fluorouracil, *Int. J. Pharm.*, 2017, **516**, 61–70.

22 K. S. Cho, S. J. Hong, M. H. Ahn, S. Pal, P. H. Choung, J. Sangshetti and R. B. Arote, Targeted delivery of siRNA therapeutics using ligand mediated biodegradable polymeric nanocarriers, *Curr. Pharm. Des.*, 2018, **24**, 1788–1800.

23 A. Baker, M. S. Khan, M. Z. Iqbal and M. S. Khan, Tumor-targeted drug delivery by nanocomposites, *Curr. Drug Metab.*, 2020, **21**, 599–613.

24 J. Majumder and T. Minko, Multifunctional and stimuli-responsive nanocarriers for targeted therapeutic delivery, *Expert Opin. Drug Delivery*, 2020, **1**, 23.

25 H. Li, J. Sun, H. Zhu, H. Wu, H. Zhang, Z. Gu and K. Luo, Recent advances in development of dendritic polymer-based nanomedicines for cancer diagnosis, *Wiley Interdiscip. Rev.: Nanomed. Nanobiotechnol.*, 2020, e1670.

26 J. L. Arias, Liposomes in drug delivery: a patent review (2007–present), *Expert Opin. Ther. Pat.*, 2013, **23**, 1399–1414.

27 V. Jain, H. Kumar, H. V. Anod, P. Chand, N. V. Gupta, S. Dey and S. S. Kesharwani, A review of nanotechnology-based approaches for breast cancer and triple-negative breast cancer, *J. Controlled Release*, 2020, **326**, 628–647.

28 J. D. Durán, J. L. Arias, V. Gallardo and A. V. Delgado, Magnetic colloids as drug vehicles, *J. Pharm. Sci.*, 2008, **97**, 2948–2983.

29 L. H. Reddy, J. L. Arias, J. Nicolas and P. Couvreur, Magnetic nanoparticles: design and characterization, toxicity and biocompatibility, pharmaceutical and biomedical applications, *Chem. Rev.*, 2012, **112**, 5818–5878.

30 M. M. El-Hammadi and J. L. Arias, Iron oxide-based multifunctional nanoparticulate systems for biomedical applications: a patent review (2008 – present), *Expert Opin. Ther. Pat.*, 2015, **25**, 691–709.

31 P. Das, M. Colombo and D. Prosperi, Recent advances in magnetic fluid hyperthermia for cancer therapy, *Colloids Surf., B*, 2019, **174**, 42–55.

32 T. L. Kalber, K. L. Ordidge, P. Southern, M. R. Loebinger, P. G. Kyrtatos, Q. A. Pankhurst, M. F. Lythgoe and S. M. Janes, Hyperthermia treatment of tumors by mesenchymal stem cell-delivered superparamagnetic iron oxide nanoparticles, *Int. J. Nanomed.*, 2016, **11**, 1973–1983.

33 Z. Bakhtiary, A. A. Saei, M. J. Hajipour, M. Raoufi, O. Vermesh and M. Mahmoudi, Targeted superparamagnetic iron oxide nanoparticles for early detection of cancer: Possibilities and challenges, *Nanomedicine*, 2016, **12**, 287–307.

34 D. J. M. de Gouw, M. C. Maas, C. Slagt, J. Mühling, A. Nakamoto, B. R. Klarenbeek, C. Rosman, J. J. Hermans and T. W. J. Scheenen, Controlled mechanical ventilation to detect regional lymph node metastases in esophageal cancer using USPIO-enhanced MRI; comparison of image quality, *Magn. Reson. Imaging*, 2020, **74**, 258–265.

35 J. L. Arias, Advanced methodologies to formulate nanotheragnostic agents for combined drug delivery and imaging, *Expert. Opin. Drug Delivery*, 2011, **8**, 1589–1608.

36 S. M. Dadfar, K. Roemhild, N. I. Drude, S. von Stillfried, R. Knüchel, F. Kiessling and T. Lammers, Iron oxide nanoparticles: diagnostic, therapeutic and theranostic applications, *Adv. Drug Delivery Rev.*, 2019, **138**, 302–325.

37 J. L. Arias, L. H. Reddy and P. Couvreur, Fe_3O_4/chitosan nanocomposite for magnetic drug targeting to cancer, *J. Mater. Chem.*, 2012, **22**, 7622–7632.

38 G. García-García, F. Fernández-Álvarez, L. Cabeza, A. V. Delgado, C. Melguizo, J. C. Prados and J. L. Arias, Gemcitabine-Loaded Magnetically Responsive Poly(ε-caprolactone) Nanoparticles against Breast Cancer, *Polymers*, 2020, **12**, 2790.

39 M. Muñoz de Escalona, E. Sáez-Fernández, J. C. Prados, C. Melguizo and J. L. Arias, Magnetic solid lipid nanoparticles in hyperthermia against colon cancer, *Int. J. Pharm.*, 2016, **504**, 11–19.

40 C. Lorente, L. Cabeza, B. Clares, R. Ortiz, L. Halbaut, A. V. Delgado, G. Perazzoli, J. Prados, J. L. Arias and C. Melguizo, Formulation and in vitro evaluation of magnetoliposomes as a potential nanotool in colorectal cancer therapy, *Colloids Surf., B*, 2018, **171**, 553–565.

4976 | *J. Mater. Chem. B*, 2021, **9**, 4963–4980

This journal is © The Royal Society of Chemistry 2021

41 B. Pérez-Artacho, V. Gallardo, M. A. Ruiz and J. L. Arias, Maghemite/poly(d,l-lactide-co-glycolyde) composite nanoplatform for therapeutic applications, *J. Nanopart. Res.*, 2012, **14**, 768.

42 Y. N. Cui, Q. X. Xu, P. Davoodi, D. P. Wang and C. H. Wang, Enhanced intracellular delivery and controlled drug release of magnetic PLGA nanoparticles modified with transferrin, *Acta Pharmacol. Sin.*, 2017, **38**, 943–953.

43 H. A. Chen, Y. H. Ma, T. Y. Hsu and J. P. Chen, Preparation of peptide and recombinant tissue plasminogen activator conjugated poly(lactic-co-glycolic acid) (PLGA) magnetic nanoparticles for dual targeted thrombolytic therapy, *Int. J. Mol. Sci.*, 2020, **21**, 2690.

44 G. K. Jain, S. A. Pathan, S. Akhter, N. Ahmad, N. Jain, S. Talegaonkar, R. K. Khar and F. J. Ahmad, Mechanistic study of hydrolytic erosion and drug release behaviour of PLGA nanoparticles: influence of chitosan, *Polym. Degrad. Stab.*, 2010, **95**, 2360–2366.

45 R. Domínguez-Ríos, D. R. Sánchez-Ramírez, K. Ruiz-Saray, P. E. Oceguera-Basurto, M. Almada, J. Juárez, A. Zepeda-Moreno, A. Del Toro-Arreola, A. Topete and A. Daneri-Navarro, Cisplatin-loaded PLGA nanoparticles for HER2 targeted ovarian cancer therapy, *Colloids Surf., B*, 2019, **178**, 199–207.

46 M. Dunne, I. Corrigan and Z. Ramtoola, Influence of particle size and dissolution conditions on the degradation properties of polylactide-co-glycolide particles, *Biomaterials*, 2000, **21**, 1659–1668.

47 S. Lappe, D. Mulac and K. Langer, Polymeric nanoparticles - Influence of the glass transition temperature on drug release, *Int. J. Pharm.*, 2017, **517**, 338–347.

48 K. Park, A. Otte, F. Sharifi, J. Garner, S. Skidmore, H. Park, Y. K. Jhon, B. Qin and Y. Wang, Potential roles of the glass transition temperature of PLGA microparticles in drug release kinetics, *Mol. Pharm.*, 2021, **18**, 18–32.

49 D. P. Santos, M. A. Ruiz, V. Gallardo, M. V. B. Zanoni and J. L. Arias, Multifunctional antitumor magnetite/chitosan-l-glutamic acid (core/shell) nanocomposites, *J. Nanopart. Res.*, 2011, **13**, 4311–4323.

50 F. Assa, H. Jafarizadeh-Malmiri, H. Ajamein, H. Vaghari, N. Anarjan, O. Ahmadi and A. Berenjian, Chitosan magnetic nanoparticles for drug delivery systems, *Crit. Rev. Biotechnol.*, 2017, **37**, 492–509.

51 L. S. Arias, J. P. Pessan, F. N. de Souza Neto, B. H. R. Lima, E. R. de Camargo, G. Ramage, A. C. B. Delbem and D. R. Monteiro, Novel nanocarrier of miconazole based on chitosan-coated iron oxide nanoparticles as a nanotherapy to fight Candida biofilms, *Colloids Surf., B*, 2020, **192**, 111080.

52 B. Sarmento, D. Mazzaglia, M. C. Bonferoni, A. P. Neto, M. do Céu Monteiro and V. Seabra, Effect of chitosan coating in overcoming the phagocytosis of insulin loaded solid lipid nanoparticles by mononuclear phagocyte system, *Carbohydr. Polym.*, 2011, **84**, 919–925.

53 S. A. Abouelmagd, Y. J. Ku and Y. Yeo, Low molecular weight chitosan-coated polymeric nanoparticles for sustained and pH-sensitive delivery of paclitaxel, *J. Drug Targeting*, 2015, **23**, 725–735.

54 D. Chirio, E. Peira, S. Sapino, C. Dianzani, A. Barge, E. Muntoni, S. Morel and M. Gallarate, Stearoyl-chitosan coated nanoparticles obtained by microemulsion cold dilution technique, *Int. J. Mol. Sci.*, 2018, **19**, 3833.

55 R. A. Ishak, G. A. Awad, N. M. Zaki, Ael-H El-Shamy and N. D. Mortada, A comparative study of chitosan shielding effect on nano-carriers hydrophilicity and biodistribution, *Carbohydr. Polym.*, 2013, **94**, 669–676.

56 L. Chronopoulou, M. Massimi, M. F. Giardi, C. Cametti, L. C. Devirgiliis, M. Dentini and C. Palocci, Chitosan-coated PLGA nanoparticles: a sustained drug release strategy for cell cultures, *Colloids Surf., B*, 2013, **103**, 310–317.

57 W. Li, M. Yalcin, Q. Lin, M. M. Ardawi and S. A. Mousa, Self-assembly of green tea catechin derivatives in nanoparticles for oral lycopene delivery, *J. Controlled Release*, 2017, **248**, 117–124.

58 H. Chen, W. Yang, H. Chen, L. Liu, F. Gao, X. Yang, Q. Jiang, Q. Zhang and Y. Wang, Surface modification of mitoxantrone-loaded PLGA nanospheres with chitosan, *Colloids Surf., B*, 2009, **73**, 212–218.

59 S. Kashyap, A. Singh, A. Mishra and V. Singh, Enhanced sustained release of furosemide in long circulating chitosan-conjugated PLGA nanoparticles, *Results Pharma Sci.*, 2019, **14**, 93–106.

60 B. Lu, X. Lv and Y. Le, Chitosan-modified PLGA nanoparticles for control-released drug delivery, *Polymers*, 2019, **11**, 304.

61 K. Tahara, H. Yamamoto, N. Hirashima and Y. Kawashima, Chitosan-modified poly(D,L-lactide-co-glycolide) nanospheres for improving siRNA delivery and gene-silencing effects, *Eur. J. Pharm. Biopharm.*, 2010, **74**, 421–426.

62 Z. G. Yue, W. Wei, P. P. Lv, H. Yue, L. Y. Wang, Z. G. Su and G. H. Ma, Surface Charge Affects Cellular Uptake and Intracellular Trafficking of Chitosan-Based Nanoparticles, *Biomacromolecules*, 2011, **12**, 2440–2446.

63 S. H. Voon, S. X. Tiew, C. S. Kue, H. B. Lee, L. V. Kiew, M. Misran, A. Kamkaew, K. Burgess and L. Y. Chung, Chitosan-coated poly(lactic-co-glycolic acid)-diiodinated boron-dipyrromethene nanoparticles improve tumor selectivity and stealth properties in photodynamic cancer therapy, *J. Biomed. Nanotechnol.*, 2016, **12**, 1431–1452.

64 A. Babu, N. Amreddy, R. Muralidharan, G. Pathuri, H. Gali, A. Chen, Y. D. Zhao, A. Munshi and R. Ramesh, Chemodrug delivery using integrin-targeted PLGA-Chitosan nanoparticle for lung cancer therapy, *Sci. Rep.*, 2017, **7**, 14674.

65 M. M. Badran, A. H. Alomrani, G. I. Harisa, A. E. Ashour, A. Kumar and A. E. Yassin, Novel docetaxel chitosan-coated PLGA/PCL nanoparticles with magnified cytotoxicity and bioavailability, *Biomed. Pharmacother.*, 2018, **106**, 1461–1468.

66 S. Caban-Toktas, A. Sahin, S. Lule, G. Esendagli, I. Vural, K. Karlı Oguz, F. Soylemezoglu, M. Mut, T. Dalkara, M. Khan and Y. Capan, Combination of paclitaxel and R-flurbiprofen loaded PLGA nanoparticles suppresses

This journal is © The Royal Society of Chemistry 2021

J. Mater. Chem. B, 2021, **9**, 4963–4980 | **4977**

glioblastoma growth on systemic administration, *Int. J. Pharm.*, 2020, **578**, 119076.

67 V. Cricchio, M. Best, E. Reverchon, N. Maffulli, G. Phillips, M. Santin and G. Della Porta, Novel superparamagnetic microdevices based on magnetized PLGA/PLA microparticles obtained by supercritical fluid emulsion and coating by carboxybetaine-functionalized chitosan allowing the tuneable release of therapeutic, *J. Pharm. Sci.*, 2017, **106**, 2097–2105.

68 A. Shanavas, S. Sasidharan, D. Bahadur and R. Srivastava, Magnetic core-shell hybrid nanoparticles for receptor targeted anti-cancer therapy and magnetic resonance imaging, *J. Colloid Interface Sci.*, 2017, **486**, 112–120.

69 G. Li, Y. Wang and G. Tan, The construction of EpCAM/vimentin-PLGA/lipid immunomagnetic microspheres and the isolation of circulating tumor cells from lung cancer, *Int. J. Clin. Exp. Pathol.*, 2018, **11**, 5561–5570.

70 R. Massart, Preparation of Aqueous Magnetic Liquids in Alkaline and Acidic Media, *IEEE Trans. Magn.*, 1981, **17**, 1247–1248.

71 A. Bee, R. Massart and S. Neveu, Synthesis of very fine maghemite particles, *J. Magn. Magn. Mater.*, 1995, **149**, 6–9.

72 L. N. Okassa, H. Marchais, L. Douziech-Eyrolles, K. Hervé, S. Cohen-Jonathan, E. Munnier, M. Soucé, C. Linassier, P. Dubois and I. Chourpa, Optimization of iron oxide nanoparticles encapsulation within poly(D,L-lactide-*co*-glycolide) sub-micron particles, *Eur. J. Pharm. Biopharm.*, 2007, **67**, 31–38.

73 T. J. Matshaya, A. E. Lanterna, A. M. Granados, R. W. Krause, B. Maggio and R. V. Vico, Distinctive interactions of oleic acid covered magnetic nanoparticles with saturated and unsaturated phospholipids in Langmuir monolayers, *Langmuir*, 2014, **30**, 5888–5896.

74 J. Ibarra, J. Melendres, M. Almada, M. G. Burboa, P. Taboada, J. Juárez and M. A. Valdez, Synthesis and characterization of magnetite/PLGA/chitosan nanoparticles, *Mater. Res. Express*, 2015, **2**, 1–17.

75 M. A. Holgado, J. Alvarez-Fuentes, M. Fernández-Arévalo and J. L. Arias, Possibilities of poly(d,l-lactide-*co*-glycolide) in the formulation of nanomedicines against cancer, *Curr. Drug Targets*, 2011, **12**, 1096–1111.

76 L. Martín-Banderas, I. Muñoz-Rubio, J. Álvarez-Fuentes, M. Durán-Lobato, J. L. Arias, M. Á. Holgado and M. Fernández-Arévalo, Engineering of Δ9-tetrahydrocannabinol delivery systems based on surface modified-PLGA nanoplatforms, *Colloids Surf., B*, 2014, **123**, 114–122.

77 J. L. Arias, M. López-Viota, V. Gallardo and M. A. Ruiz, Chitosan nanoparticles as a new delivery system for the chemotherapy agent tegafur, *Drug Dev. Ind. Pharm.*, 2010, **36**, 744–750.

78 J. L. Arias, L. H. Reddy and P. Couvreur, Superior preclinical efficacy of gemcitabine developed as chitosan nanoparticulate system, *Biomacromolecules*, 2011, **12**, 97–104.

79 J. D. Unciti-Broceta, J. L. Arias, J. Maceira, M. Soriano, M. Ortiz-González, J. Hernández-Quero, M. Muñóz-Torres, H. P. de Koning, S. Magez and J. A. Garcia-Salcedo, Specific Cell Targeting Therapy Bypasses Drug Resistance Mechanisms in African Trypanosomiasis, *PLoS Pathog.*, 2015, **11**, e1004942.

80 H. L. Andersen, M. Saura-Múzquiz, C. Granados-Miralles, E. Canévet, N. Lock and M. Christensen, Crystalline and magnetic structure-property relationship in spinel ferrite nanoparticles, *Nanoscale*, 2018, **10**, 14902–14914.

81 M. Di Marco, C. Sadun, M. Port, I. Guilbert, P. Couvreur and C. Dubernet, Physicochemical characterization of ultrasmall superparamagnetic iron oxide particles (USPIO) for biomedical application as MRI contrast agents, *Int. J. Nanomed.*, 2007, **2**, 609–622.

82 M. Pernia Leal, C. Caro and M. L. García-Martín, Shedding light on zwitterionic magnetic nanoparticles: limitations for in vivo applications, *Nanoscale*, 2017, **9**, 8176–8184.

83 V. Nica, C. Caro, J. M. Páez-Muñoz, M. Pernia Leal and M. L. Garcia-Martin, Bi-magnetic core-shell CoFe$_2$O$_4$@MnFe$_2$O$_4$ nanoparticles for *in vivo* theranostics, *Nanomaterials*, 2020, **10**, 907.

84 J. L. Arias, M. López-Viota, E. Sáez-Fernández, M. A. Ruiz and A. V. Delgado, Engineering of an antitumor (core/shell) magnetic nanoformulation based on the chemotherapy agent ftorafur, *Colloids Surf., A*, 2011, **384**, 157–163.

85 B. C. Dash, G. Réthoré, M. Monaghan, K. Fitzgerald, W. Gallagher and A. Pandit, The influence of size and charge of chitosan/polyglutamic acid hollow spheres on cellular internalization, viability and blood compatibility, *Biomaterials*, 2010, **31**, 8188–8197.

86 International Organization for Standardization. 2009. Biological evaluation of medical devices - part 5: tests for *in vitro* cytotoxicity (ISO 10993-5:2009).

87 B. Clares, R. A. Biedma-Ortiz, E. Sáez-Fernández, J. C. Prados, C. Melguizo, L. Cabeza, R. Ortiz and J. L. Arias, Nano-engineering of 5-fluorouracil-loaded magnetoliposomes for combined hyperthermia and chemotherapy against colon cancer, *Eur. J. Pharm. Biopharm.*, 2013, **85**, 329–338.

88 R. Hergt and S. Dutz, Magnetic particle hyperthermia–biophysical limitations of a visionary tumour therapy, *J. Magn. Magn. Mater.*, 2007, **311**, 187–192.

89 A. P. Khandhar, R. M. Ferguson, J. A. Simon and K. M. Krishnan, Tailored magnetic nanoparticles for optimizing magnetic fluid hyperthermia, *J. Biomed. Mater. Res., Part A*, 2012, **100**, 728–737.

90 E. Fantechi, C. Innocenti, M. Zanardelli, M. Fittipaldi, E. Falvo, M. Carbo, V. Shullani, L. Di Cesare Mannelli, C. Ghelardini, A. M. Ferretti, A. Ponti, C. Sangregorio and P. Ceci, A smart platform for hyperthermia application in cancer treatment: cobalt-doped ferrite nanoparticles mineralized in human ferritin cages, *ACS Nano*, 2014, **8**, 4705–4719.

91 C. Caro, C. M. Muñoz-Hernández, M. Pernia Leal and M. L. García-Martín, In vivo pharmacokinetics of magnetic nanoparticles, *Methods. Mol. Biol.*, 2018, **1718**, 409–419.

92 C. Caro, D. Egea-Benavente, R. Polvillo, J. L. Royo, M. Pernia Leal and M. L. García-Martín, Comprehensive

4978 | *J. Mater. Chem. B*, 2021, **9**, 4963–4980

This journal is © The Royal Society of Chemistry 2021

toxicity assessment of PEGylated magnetic nanoparticles for in vivo applications, *Colloids Surf., B*, 2019, **177**, 253–259.

93 H. Maeda, J. Wu, T. Sawa, Y. Matsumura and K. Hori, Tumor vascular permeability and the EPR effect in macromolecular therapeutics: a review, *J. Controlled Release*, 2000, **65**, 271–284.

94 M. Gaumet, A. Vargas, R. Gurny and F. Delie, Nanoparticles for drug delivery: the need for precision in reporting particle size parameters, *Eur. J. Pharm. Biopharm.*, 2008, **69**, 1–9.

95 C. He, Y. Hu, L. Yin, C. Tang and C. Yin, Effects of particle size and surface charge on cellular uptake and biodistribution of polymeric nanoparticles, *Biomaterials*, 2010, **31**, 3657–3666.

96 X. Liu, N. Huang, H. Li, Q. Jin and J. Ji, Surface and size effects on cell interaction of gold nanoparticles with both phagocytic and nonphagocytic cells, *Langmuir*, 2013, **29**, 9138–9148.

97 J. L. Arias, M. A. Ruiz, V. Gallardo and A. V. Delgado, Tegafur loading and release properties of magnetite/poly-(alkylcyanoacrylate) (core/shell) nanoparticles, *J. Controlled Release*, 2008, **125**, 50–58.

98 J. L. Arias, V. Gallardo, M. A. Ruiz and A. V. Delgado, Magnetite/poly(alkylcyanoacrylate) (core/shell) nanoparticles as 5-Fluorouracil delivery systems for active targeting, *Eur. J. Pharm. Biopharm.*, 2008, **69**, 54–63.

99 S. Nasrazadani and S. Hassani, in *Handbook of Materials Failure Analysis with Case Studies from the Oil and Gas Industry*, ed. A. S. H. Makhlouf and M. Aliofkhazraei, Butterworth-Heinemann, Oxford, 2016, vol. 2, pp. 39–54.

100 M. A. Holgado, M. J. Cózar-Bernal, S. Salas, J. L. Arias, J. Alvarez-Fuentes and M. Fernández-Arévalo, Protein-loaded PLGA microparticles engineered by flow focusing: physicochemical characterization and protein detection by reversed-phase HPLC, *Int. J. Pharm.*, 2009, **380**, 147–154.

101 R. Di Corato, A. Aloisi, S. Rella, J. M. Greneche, G. Pugliese, T. Pellegrino, C. Malitesta and R. Rinaldi, Maghemite Nanoparticles with Enhanced Magnetic Properties: One-Pot Preparation and Ultrastable Dextran Shell, *ACS Appl. Mater. Interfaces*, 2018, **10**, 20271–20280.

102 J. Depeyrot, E. C. Sousa, R. Aquino, F. A. Tourinho, E. Dubois, J. C. Bacri and R. Perzynski, Rare earth doped maghemite EDL-MF: a perspective for nanoradiotherapy?, *J. Magn. Magn. Mater.*, 2002, **252**, 375–377.

103 Y. Ling, M. Long, P. Hu, Y. Chen and J. Huang, Magnetically separable core-shell structural γ-Fe$_2$O$_3$@Cu/Al-MCM-41 nanocomposite and its performance in heterogeneous Fenton catalysis, *J. Hazard. Mater.*, 2014, **264**, 195–202.

104 S. Narimani-Sabegh and E. Noroozian, Magnetic solid-phase extraction and determination of ultra-trace amounts of antimony in aqueous solutions using maghemite nanoparticles, *Food Chem.*, 2019, **287**, 382–389.

105 I. Berry, S. Benderbous, J. P. Ranjeva, D. Gracia-Meavilla, C. Manelfe and D. Le Bihan, Contribution of Sinerem used

as blood-pool contrast agent: detection of cerebral blood volume changes during apnea in the rabbit, *Magn. Reson. Med.*, 1996, **36**, 415–419.

106 S. Laurent, D. Forge, M. Port, A. Roch, C. Robic, L. Vander Elst and R. N. Muller, Magnetic iron oxide nanoparticles: synthesis, stabilization, vectorization, physicochemical characterizations, and biological applications, *Chem. Rev.*, 2008, **108**, 2064–2110.

107 G. B. Toth, C. G. Varallyay, A. Horvath, M. R. Bashir, P. L. Choyke, H. E. Daldrup-Link, E. Dosa, J. P. Finn, S. Gahramanov, M. Harisinghani, I. Macdougall, A. Neuwelt, S. S. Vasanawala, P. Ambady, R. Barajas, J. S. Cetas, J. Ciporen, T. J. DeLoughery, N. D. Doolittle, R. Fu, J. Grinstead, A. R. Guimaraes, B. E. Hamilton, X. Li, H. L. McConnell, L. L. Muldoon, G. Nesbit, J. P. Netto, D. Petterson, W. D. Rooney, D. Schwartz, L. Szidonya and E. A. Neuwelt, Current and potential imaging applications of ferumoxytol for magnetic resonance imaging, *Kidney Int.*, 2017, **92**, 47–66.

108 P. Caravan, J. J. Ellison, T. J. McMurry and R. B. Lauffer, Gadolinium(III) chelates as MRI contrast agents: structure, dynamics, and applications, *Chem. Rev.*, 1999, **99**, 2293–2352.

109 A. Pandey, N. Dhas, P. Deshmukh, C. Caro, P. Patil, M. L. García-Martín, B. Padya, A. Nikam, T. Mehta and S. Mutalik, Heterogeneous surface architectured metal-organic frameworks for cancer therapy, imaging, and biosensing: a state-of-the-art review, *Coord. Chem. Rev.*, 2020, **409**, 213212.

110 S. Fucharoen and V. Viprakasit, Hb H disease: clinical course and disease modifiers, *Hematology Am. Soc. Hematol. Educ. Program.*, 2009, **26**, 34.

111 P. I. Soares, I. M. Ferreira, R. A. Igreja, C. M. Novo and J. P. Borges, Application of hyperthermia for cancer treatment: recent patents review, *Recent Pat. Anti-Cancer Drug Discovery*, 2012, **7**, 64–73.

112 L. Beola, L. Asín, R. M. Fratila, V. Herrero, J. M. de la Fuente, V. Grazú and L. Gutiérrez, Dual role of magnetic nanoparticles as intracellular hotspots and extracellular matrix disruptors triggered by magnetic hyperthermia in 3D cell culture models, *ACS Appl. Mater. Interfaces*, 2018, **10**, 44301–44313.

113 R. Gupta and D. Sharma, Biofunctionalization of magnetite nanoparticles with stevioside: effect on the size and thermal behaviour for use in hyperthermia applications, *Int. J. Hyperthermia*, 2019, **36**, 302–312.

114 S. Dutz and R. Hergt, Magnetic particle hyperthermia--a promising tumour therapy?, *Nanotechnology*, 2014, **25**, 452001.

115 M. Kettering, I. Grau, N. Pömpner, M. Stapf, M. Gajda, U. Teichgräber and I. Hilger, Means to increase the therapeutic efficiency of magnetic heating of tumors, *Biomed. Technol.*, 2015, **60**, 505–517.

116 S. L. Easo and P. V. Mohanan, Dextran stabilized iron oxide nanoparticles: synthesis, characterization and in vitro studies, *Carbohydr. Polym.*, 2013, **92**, 726–732.

This journal is © The Royal Society of Chemistry 2021

J. Mater. Chem. B, 2021, **9**, 4963–4980 | **4979**

117 S. V. Jadhav, P. S. Shewale, B. C. Shin, M. P. Patil, G. D. Kim, A. A. Rokade, S. S. Park, R. A. Bohara and Y. S. Yu, Study of structural and magnetic properties and heat induction of gadolinium-substituted manganese zinc ferrite nanoparticles for in vitro magnetic fluid hyperthermia, *J. Colloid Interface Sci.*, 2019, **541**, 192–203.

118 S. Y. Lee, E. Jung, J. H. Park, J. W. Park, C. K. Shim, D. D. Kim, I. S. Yoon and H. J. Cho, Transient aggregation of chitosan-modified poly(D,L-lactic-*co*-glycolic) acid nanoparticles in the blood stream and improved lung targeting efficiency, *J. Colloid Interface Sci.*, 2016, **480**, 102–108.

4980 | *J. Mater. Chem. B*, 2021, **9**, 4963–4980

This journal is © The Royal Society of Chemistry 2021